Thermal and chemical evolution of Venus and super-Venus planets

Joseph G. O'Rourke
Adviser: Jun Korenaga
Additional Readers: David Bercovici and Debra Fischer

April 27, 2012

A Senior Thesis presented to the faculty of the Departments of Geology & Geophysics and Astronomy, Yale University, in partial fulfillment of the Bachelor's Degree

Summary

The ongoing discovery of terrestrial exoplanets accentuates the importance of understanding planetary evolution for a wide range of initial conditions. In Part I of this thesis, thermal evolution simulations are performed to investigate the evolution of Mars, Venus, and putative super-Venus planets in the stagnant-lid regime, the most natural mode of convection with strongly temperature-dependent viscosity. We employ principal component analysis and linear regression to capture the first-order systematics of possible evolutionary scenarios from a large number of simulation runs. With increased planetary mass, crustal thickness and the degree of mantle processing are both predicted to decrease, and such size effects can also be derived with simple scaling analyses. The likelihood of plate tectonics is quantified using a mantle rheology that takes into account both ductile and brittle deformation mechanisms. Confirming earlier scaling analyses, the effects of lithosphere hydration dominate the effects of planetary mass. The possibility of basalt-eclogite phase transition in the planetary crust is found to increase with planetary mass, and we suggest that massive terrestrial planets may escape the stagnant-lid regime through the formation of a self-destabilizing dense eclogite layer.

Spacecraft observations allow the evolution of Venus to be further constrained. In Part II of this thesis, we begin to search for a model that predicts the present-day atmospheric mass of radiogenic argon and explains why the surface of Venus is almost uniformly young-looking. We consider two end-member scenarios: a single catastrophic resurfacing event and continuous evolution in the stagnant-lid regime. With a simple model of closed-system mantle evolution, we predict the range of crustal thicknesses that may have been produced during a rapid resurfacing event. We modify our parametrized simulations to track the mass transport of argon and to include a simple model of upwelling mantle plumes. Sensitivity analyses and linear regression are used to quantify the range of initial conditions that will produce desired values for key model output parameters. Compared to the catastrophic resurfacing model, smaller crustal thicknesses are required to yield the measured magnitude of argon degassing. Mantle plumes have negligible effects on the global argon budget, but may be important to understanding the surface geology of Venus. We find a wide range of initial conditions that satisfy observational constraints and produce plume upwelling at the assumed time of global resurfacing.

Contents

Part I
Size effects and the formation of self-destabilizing crust

1 Introduction

Plate tectonics is only observed on Earth and is likely important to Earth's uniquely clement surface conditions (e.g., Kasting and Catling, 2003). Other terrestrial planets in the Solar System (i.e., Mercury, Mars, and Venus) are generally considered to feature a rigid spherical shell encompassing the entire planet, with hot mantle convecting beneath the shell (e.g., Schubert et al., 2001). This mode of mantle convection is known as stagnant-lid convection. In fact, stagnant-lid convection may be most natural for planetary mantles because the viscosity of constituent materials is strongly temperature-dependent (Solomatov, 1995). With the discovery of many extrasolar terrestrial planets with mass 1 to $10M_{\oplus}$ (e.g., Rivera et al., 2005; Udry et al., 2007; Queloz et al., 2009; Mayor et al., 2009; Léger et al., 2009; Charbonneau et al., 2009; Borucki et al., 2011), understanding planetary evolution in the stagnant-lid regime is critical.

Parametrized models of stagnant-lid convection have long been applied to planets in our Solar System in an effort to infer likely planetary evolution scenarios from limited observational constraints (e.g., Stevenson et al., 1983; Spohn, 1991; Hauck and Phillips, 2002; Fraeman and Korenaga, 2010). Previous studies of massive terrestrial planets are more theoretical in nature, focusing on two broad questions. First, the effects of planetary mass on the likelihood of plate tectonics have been studied through scaling analyses and simple parametrized convection models (Valencia et al., 2007; O'Neill and Lenardic, 2007; Korenaga, 2010a; van Heck and Tackley, 2011). Second, the evolution of planets in the stagnant-lid regime has been contrasted with evolution with plate tectonics in the hope of identifying atmospheric signatures that would indicate the regime of mantle convection for a distant planet (e.g., Kite et al., 2009). Mantle dynamics in the stagnant-lid regime, however, can be more complex than previously thought owing to the effects of mantle processing and crustal formation, and the scaling law of stagnant-lid convection that takes such complications into account has been developed only recently (Korenaga, 2009). It is thus warranted to take a fresh look at the fate of massive terrestrial planets in the stagnant-lid regime and to explore the general effects of initial conditions including planetary mass.

This study extends a parametrized model of stagnant-lid convection recently applied to Mars (Fraeman and Korenaga, 2010) to terrestrial planets of various masses, including massive planets that evolve in the stagnant-lid regime, which are termed "super-Venus" planets. This model incorporates the effects of compositional buoyancy and dehydration stiffening on mantle dynamics (Korenaga, 2009), which are rarely accounted for except in simulations of plate tectonics. Unlike in previous studies, sensitivity analyses are extensively performed to quantify the relationship between initial conditions and modeling results. Principal component analysis is used to simplify the interpretation of a large number of simulation results. Simple scaling analyses are also conducted to derive a theoretical basis for major modeling results. Moreover, the likelihood of plate tectonics is quantified by tracking the viscosity contrast across the lithosphere during each simulation.

The evolution of a particular planet is likely to diverge from the predictions of these simple parametrized models. Few constraints are available beyond planetary mass and radius for extrasolar terrestrial planets. But for terrestrial planets in our Solar System, more data are available from decades of observations and spacecraft visits. The purpose of this study is to explore hypothetical planetary evolution with the simplest assumptions on mantle dynamics, thereby serving as a reference model on which additional complications may be considered if necessary.

2 Theoretical formulation

Parametrized convection models are used to simulate the evolution of Mars, Venus, and super-Venus planets for a wide range of initial conditions. Simulations for Mars and Venus are not intended to precisely reconstruct the histories of these planets, but instead aim to explore the general paths along which these planets could have evolved in the stagnant-lid regime. Equations used to track the thermal and chemical evolution of terrestrial planets are taken from Fraeman and Korenaga (2010) with some modifications. Earth-like, peridotite mantle compositions are used to parametrize melting behavior. Although continuous evolution in the stagnant-lid regime is assumed, a simple model of lithospheric weakening is also considered to evaluate the likelihood of plate tectonics occurring at some point during planetary evolution.

2.1 Governing equations

Mars, Venus, and putative super-Venus planets are assumed to begin as differentiated bodies with a mantle and core. Energy conservation yields two governing equations. First, the energy balance for the core is

$$[4\pi R_i^2 \rho_c (L_c + E_g)\frac{dR_i}{dT_{cm}} - \frac{4}{3}\pi R_c^3 \rho_c C_c \eta_c]\frac{dT_{cm}}{dt} = 4\pi R_c^2 F_c, \quad (1)$$

where R_c and R_i are the radii of the core and inner core, respectively; ρ_c is the density of the core; L_c is the latent heat of solidification associated with the inner core; E_g is the gravitational energy liberated per unit mass of the inner core; η_c is the ratio of T_{cm}, the temperature at the core side of the core/mantle boundary, to the average core temperature; C_c is the specific heat of the core; and F_c is the heat flux out of the core. The formulation of core cooling is identical to that of Stevenson et al. (1983).

Second, the energy balance for the mantle is (Hauck and Phillips, 2002)

$$\frac{4}{3}(R_m^3 - R_c^3)\left(Q_m - \rho_m C_m \eta_m \frac{dT_u}{dt}\right) - \rho_m f_m L_m = 4\pi(R_m^2 F_m - R_c^2 F_c), \quad (2)$$

where R_m is the radius of the mantle; Q_m is the volumetric heat production of the mantle; ρ_m is the density of the mantle; C_m is the specific heat of the mantle; η_m is the ratio of the average temperature of the mantle to T_u, the potential temperature of the mantle (a hypothetical temperature of the mantle adiabatically brought up to the surface without melting); f_m is volumetric melt production with associated latent heat release, L_m; and F_m is the heat flux across the mantle/crust boundary.

Some of the above parameters are universal constants, but most are planet-specific. Many important parameters are also time-varying. In particular, mantle melt is extracted to form crust, causing R_m to decrease with time. Likewise, Q_m decreases with time because of radioactive decay with some approximated average decay constant, λ (Stevenson et al., 1983), and extraction through mantle processing.

Figure 1 illustrates the assumed thermal and chemical structure in our model. Over time, melting processes an upper region of the original primitive mantle (PM) to form the crust and the depleted mantle lithosphere (DML). In parallel, the mantle lithosphere (ML), which is always thicker than the DML, develops as a conductive thermal boundary layer underlying the crust. As part of the DML can potentially delaminate and be mixed with

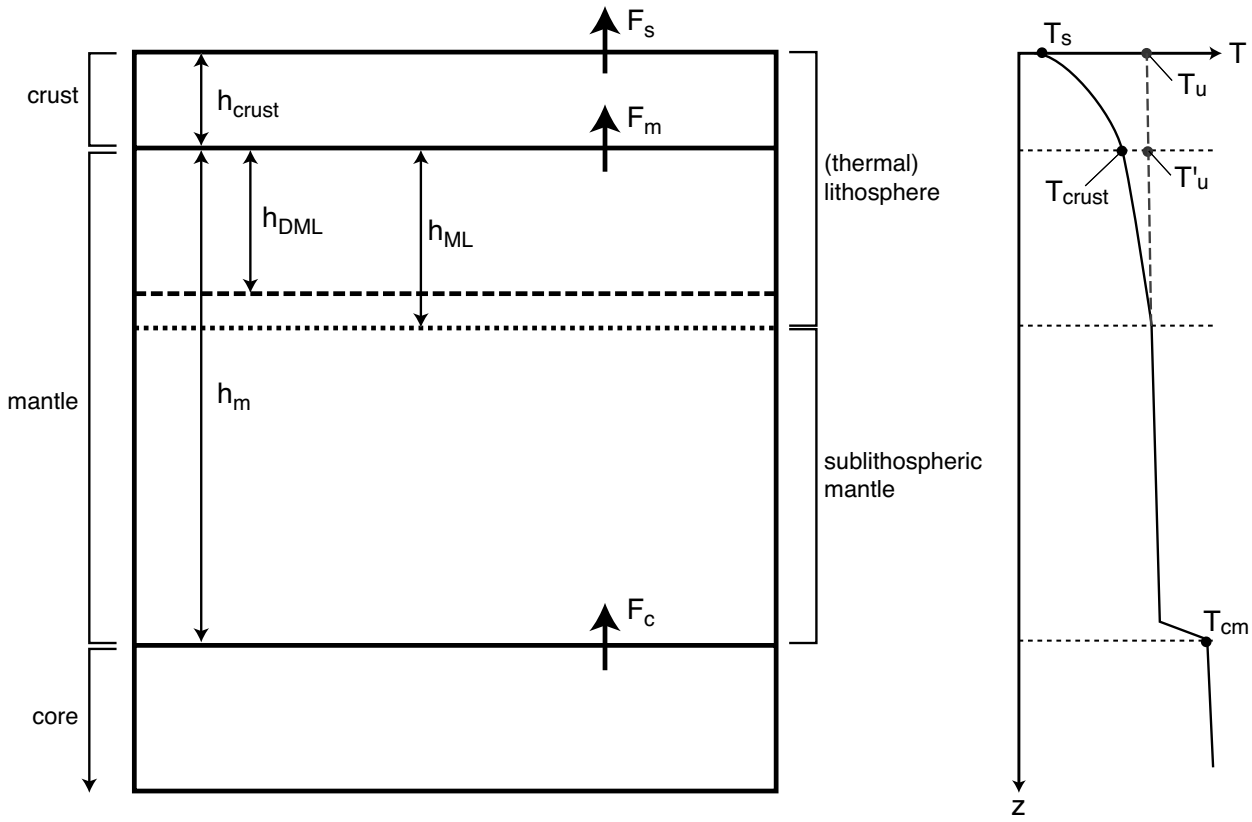

Figure 1: Cartoons showing the assumed thermal and chemical structure of terrestrial planets taken from Fraeman and Korenaga (2010). In general, terrestrial planets are divided into a crust, mantle, and core, as shown in the left panel. Mantle that has been processed by melting and stays in the thermal boundary layer is depleted mantle lithosphere (DML). The thickness of the DML must always be equal to or less than the thickness of the mantle lithosphere (ML). The section of the mantle below the thermal boundary layer is the sublithospheric mantle. The right panel shows the horizontally-averaged temperature distribution. Key model parameters are also indicated.

the convecting mantle, the composition of the convecting mantle can be more depleted than that of the PM. The mantle below the DML is thus referred to as the source mantle (SM), the composition of which is initially identical to the composition of the PM but can deviate with time. The history of these layers strongly depends on convective vigor, effects of mantle melting, and initial conditions.

2.2 Stagnant-lid convection with mantle melting

Standard parameterizations are used for mantle rheology and the vigor of convection. Mantle viscosity is a function of mantle potential temperature and the degree of hydration as (Fraeman and Korenaga, 2010)

$$\eta(T_u, C_{SM}^W) = A \exp\left[\frac{E}{RT_u} + (1 - C_{SM}^W)\log\Delta\eta_w\right], \tag{3}$$

where A is a constant factor, E is the activation energy, R is the universal gas constant, and $\Delta\eta_w$ is the viscosity contrast between wet and dry mantle. The activation energy of 300 kJ mol^{-1} (Korenaga, 2006) is used throughout this study. The normalized water concentration in the source mantle, C_{SM}^W, has an initial value of one and decreases toward zero as mantle melting causes dehydration. The effects of mineral phase transitions on the mantle dynamics of massive terrestrial planets have been controversial. Viscosity may counter-intuitively decrease with pressure above ∼0.1 TPa (Karato, 2011) or increasing viscosity and thermal conductivity may inhibit convection (Stamenkovic et al., 2011, 2012), but these potential complications are beyond the scope of our parameterized convection model, which aims to capture first-order evolutionary scenarios using average material properties.

Two nondimensional parameters characterize thermal convection with the above viscosity formulation (Solomatov, 1995). First, the internal Rayleigh number serves to quantify potential convective vigor (Fraeman and Korenaga, 2010):

$$Ra_i = \frac{\alpha\rho_m g(T_u' - T_c)h_m^3}{\kappa\eta(T_u, C_{SM}^W)}, \tag{4}$$

where α is the coefficient of thermal expansion; κ is the thermal diffusivity; T_c and T_u' are, respectively, the temperature at the bottom of the crust (called "Moho temperature") and the mantle potential temperature defined at the top of the mantle; and h_m is the thickness of the mantle. Second, the Frank-Kamenetskii parameter is defined as (Solomatov, 1995; Fraeman and Korenaga, 2010)

$$\theta = \frac{E(T_u' - T_c)}{RT_u^2}. \tag{5}$$

With these two parameters, the average convective velocity beneath the stagnant-lid

may be calculated as (Solomatov and Moresi, 2000)

$$u = 0.38\frac{\kappa}{h_m}\left(\frac{Ra}{\theta}\right)^{1/2}. \tag{6}$$

To include the effects of compositional buoyancy and dehydration stiffening, the Nusselt number, which is a non-dimensional measure of convective heat flux, must be calculated with a local stability analysis at each time step (Korenaga, 2009). The symbolic functionality may be expressed as

$$Nu = f(Ra, E, T_u, T_c, h_l, h_m, \Delta\rho, \Delta\eta_m), \tag{7}$$

where $\Delta\rho$ and $\Delta\eta_m$ are the density and viscosity contrasts between the source mantle and depleted mantle, respectively, and h_l is the thickness of the depleted mantle lithosphere. The thickness of a thermal boundary layer in the mantle is then easily calculated using

$$h_{ML} = \frac{h_m}{Nu}. \tag{8}$$

The chemical evolution of the mantle strongly affects terrestrial planet evolution. To first order, partial melting of the mantle can be considered to begin at a depth where the temperature exceeds the solidus of dry peridotite, as long as the mantle is not significantly wet (Hirth and Kohlstedt, 1996). The initial pressure of melting is (Korenaga et al., 2002)

$$P_i = \frac{T_u - 1423}{1.20 \times 10^{-7} - (dT/dP)_S}, \tag{9}$$

where $(dT/dP)_S$ is the adiabatic mantle gradient, which is roughly constant for the pressure range relevant to mantle melting. Therefore, P_i should be approximately constant for any terrestrial planet with Earth-like mantle composition. Melting stops when the convective upwelling reaches the base of the mantle lithosphere. That is, the final pressure of melting is given by

$$P_f = \rho_L g(h_c + h_{ML}), \tag{10}$$

where h_c is the thicknesses of the crust; g is gravitational acceleration; and ρ_L is the density of the lithosphere. For convenience, we use the Martian ρ_m as ρ_L, noting that ρ_L should remain roughly constant whereas ρ_m, an averaged mantle parameter, increases with planetary mass because of pressure effects. If $P_f < P_i$, then melting occurs in the melting

zone between P_i and P_f, with thickness d_m and average melt fraction equal to

$$\phi = \frac{P_i - P_f}{2} \left(\frac{d\phi}{dP} \right)_S , \tag{11}$$

where $(d\phi/dP)_S$ is the melt productivity by adiabatic decompression. Volumetric melt productivity is finally parametrized as

$$f_m = \frac{2\chi d_m u \phi}{h_m} 4\pi R_m^2, \tag{12}$$

where $\chi \sim 1$ if the upwelling mantle is cylindrical and all downwelling occurs at the cylinder's edge (Solomatov and Moresi, 2000; Fraeman and Korenaga, 2010). The crustal temperature profile is calculated as in Fraeman and Korenaga (2010), with the modification that crustal material with a temperature above $T_{crit} = 1273$ K is considered to be buoyant melt that migrates within one time step immediately below the planet's surface, producing a relatively cooler crust and a larger mantle heat flux. This modification is not important for Martian cases, because the Moho temperature does not reach the threshold except for some extreme cases, but becomes essential to achieve a realistic crustal thermal profile for larger planets.

2.3 Likelihood of plate tectonics

Thermal evolution models featuring stagnant-lid convection are not applicable to planets on which plate tectonics occurs. If a suitable weakening mechanism exists, the lithosphere may be broken into plates and recycled into the mantle. Many aspects of plate tectonics on Earth, however, are not captured in current mathematical models (Bercovici, 2003). Quantifying the conditions under which plate tectonics is favored over stagnant-lid convection is likewise difficult, and the effect of planetary mass on the likelihood of plate tectonics has been controversial (Valencia et al., 2007; Korenaga, 2010a; van Heck and Tackley, 2011). Recent studies suggest, however, that the effects of planetary mass on yield and convective stresses may be dominated by uncertainties in other important planetary parameters, such as internal heating and lithosphere hydration (Korenaga, 2010a; van Heck and Tackley, 2011).

This study uses a simple scaling that is consistent with current understanding of rock mechanics (Korenaga, 2010a), though the possibility of different lithosphere weakening mechanisms (e.g., Landuyt et al., 2008) cannot be excluded. We assume that plate tectonics

can occur if convective stress exceeds the brittle strength of lithosphere given by

$$\tau_y = c_0 + \mu\rho g z, \tag{13}$$

where c_0 is the cohesive strength, μ is the effective friction coefficient, and z is depth (Moresi and Solomatov, 1998). Experimental data indicate that the cohesive strength is negligible under lithospheric conditions, i.e., $c_0/(\mu\rho z) \ll 1$ (Byerlee, 1978). We use another non-dimensional parameter (Korenaga, 2010a):

$$\gamma = \frac{\mu}{\alpha(T_u - T_s)}, \tag{14}$$

where the relevant temperature difference is the difference between the mantle potential and surface temperatures. In the parameterized convection model formulated in the previous section, we separately consider the crust and the mantle, but when discussing the likelihood of plate tectonics using the scaling of Korenaga (2010b), it is more convenient to treat the crust and mantle together, assuming that crustal rheology is similar to mantle rheology.

Detailed scaling analyses (Korenaga, 2010a,b) show that the effective viscosity contrast across the lithosphere can be parameterized as

$$\Delta\eta_L = \exp(0.327\gamma^{0.647}\theta_{tot}), \tag{15}$$

where θ_{tot} is the Frank-Kamenetskii parameter defined using the total temperature difference explained above, i.e.,

$$\theta_{tot} = \frac{E(T_u - T_s)}{RT_u^2}. \tag{16}$$

A transition from plate-tectonic to stagnant-lid convection can take place if the above viscosity contrast exceeds a critical value

$$\Delta\eta_{L,crit} = 0.25 Ra_{i,tot}^{1/2}, \tag{17}$$

where $Ra_{i,tot}$ is defined to incorporate surface temperature as

$$Ra_{i,tot} = \frac{\alpha\rho_m g(T_u - T_s)(h_c + h_m)^3}{\kappa\eta(T_u, C_{SM}^W)}. \tag{18}$$

For each simulation, if $\min(\Delta\eta_L/\Delta\eta_{L,crit}) < 1$, then plate tectonics may have been favored at some point during the evolution of a given planet. The satisfaction of this

criterion may strongly depend on the value of μ, so a wide range of values should be tested. For silicate rocks, plausible values of μ range from 0.6 to 0.7 (Byerlee, 1978), but surface water can lower these values substantially via thermal cracking and mantle hydration (Korenaga, 2007).

2.4 Statistical analysis of simulation results

Parameterized evolution models involve quite a few model parameters. It is important to understand how simulation results depend on a particular choice of model parameters by testing a variety of situations, but at the same time, it becomes difficult to grasp the inflated amount of numerical data. Principal component analysis (PCA) can be used to assess the effective dimensionality of a given data space (Gershenfeld, 1998). Our intention here is to use PCA to extract major features and trends from a large number of simulation results. Each sensitivity analysis consists of n simulations with m output parameters, comprising a data set D_n^m. Some parameters, such as $\Delta\eta_w$ and u, exhibit orders of magnitudes of variation, and we consider their logarithms because PCA is designed for linear data sets. We normalize the data set as

$$P_n^m = \frac{D_n^m - \mu^m}{\sigma^m}, \tag{19}$$

where μ^m is the average value of the m-th output parameter,

$$\mu^m = \frac{1}{n}\sum_{i=1}^{n} D_i^m, \tag{20}$$

and σ^m is the standard deviation of the m-th output parameter,

$$\sigma^m = \left[\frac{1}{n}\sum_{i=1}^{n}(D_i^m - \mu^m)^2\right]^{1/2}. \tag{21}$$

Because the normalized data have zero mean, the covariance matrix $C_P = P^T P$ can be decomposed as $C_P = A^T \cdot \mathrm{diag}[\lambda_1 \ldots \lambda_m] \cdot A$, where λ_i, the eigenvalues, are ordered so that $\lambda_1 \geq \lambda_2 \geq \ldots \geq \lambda_m$. The corresponding eigenvectors are the principal components, which account for a progressively decreasing percentage of data variance. Principal components accounting for at least 85% (an arbitrary threshold) of the total variance are selected for examination to reveal important aspects of simulation results.

Constant	Value	Units	Ref.
λ	1.38×10^{-17}	s^{-1}	[1]
k	4.0	W m^{-1} K^{-1}	[1]
α	2×10^{-6}	K^{-1}	[1]
κ	10^{-6}	m^2 s^{-1}	[1]
ρ_L	3527	kg m^{-3}	[1]
L_m	6.0×10^5	J kg^{-1}	[2]
$L_c + E_g$	1.0×10^{-6}	J kg^{-1}	[2]
C_m	1000[a]	J kg^{-1} K^{-1}	[3]
C_c	850[a]	J kg^{-1} K^{-1}	[3]
η_m	1.3[a]	N/A	[1]
η_c	1.2[a]	N/A	[1]
$(dT/dP)_S$	1.54×10^{-8}	K Pa^{-1}	[4]
$(d\phi/dP)_S$	1.20×10^{-8}	Pa^{-1}	[4]

Table 1: Summary of universal constants used in all simulations. References: 1. Stevenson et al. (1983), 2. Fraeman and Korenaga (2010), 3. Noack et al. (2012), 4. Korenaga et al. (2002). [a]Mars has $C_m = 1149$; $C_c = 571$; $\eta_m = 1.0$; and $\eta_c = 1.1$ (Fraeman and Korenaga, 2010).

3 Numerical models

The parametrized model described above was used to calculate thermal histories of Mars, Venus, and 1 to $10M_\oplus$ super-Venus planets, where the $\oplus$ subscript denotes parameters for Earth, for a duration of 4.5 Gyr using numerical integration with a time step of 1 Myr. A wide parameter space was explored by varying the initial mantle potential temperature, $T_u(0)$; the initial core/mantle boundary temperature, $T_{cm}(0)$; the initial volumetric heat production, Q_0; the reference mantle viscosity, η_0; and the viscosity contrast between dry and wet mantle, $\Delta\eta_w$. Previous work for Mars demonstrated that simulation results were not very sensitive to the degree of compositional buoyancy and other parameters (Fraeman and Korenaga, 2010). Table 1 lists model constants common to all simulations, and Table 2 lists planet-specific ones.

3.1 Application to Mars and Venus

For Venus, the following sets of initial conditions were used: Initial mantle potential temperature, $T_u(0) = 1400$, 1550, 1700, 1850, and 2000 K; initial core/mantle boundary temperature, $T_{cm}(0) = 3500$, 4000, and 4500 K; reference viscosity, $\eta_0 = 10^{18}$, 10^{19}, and 10^{20} Pa s; and dehydration stiffening, $\Delta\eta_w = 1$, 10, and 100. For Mars, initial core/mantle

Constant	Mars	Venus	$1M_\oplus$	$2M_\oplus$	$4M_\oplus$	$5M_\oplus$	$6M_\oplus$	$8M_\oplus$	$10M_\oplus$	Units
g	3.70	8.87	10.0	13.6	18.6	20.7	22.6	26.0	29.1	m s^{-2}
T_s	220	730	300	300	300	300	300	300	300	K
R_p	3390	6050	6307	7669	9262	9821	10295	11072	11696	km
R_c	1550	3110	3295	3964	4723	4986	5206	5564	5848	km
ρ_m	3527	3551	4476	4951	5589	5845	6078	6497	6873	kg m^{-3}
ρ_c	7200	12500	12961	14882	17594	18698	19708	21530	23174	kg m^{-3}
P_{cm}	19	130	151	284	556	697	842	1144	1463	GPa
P_c	40	290	428	821	1639	2067	2508	3431	4406	GPa

Table 2: Summary of planet-specific constants for Mars, Venus, and seven super-Venus planets. Martian values were taken from Fraeman and Korenaga (2010) and references therein. Venusian values can be found in Spohn (1991) and Noack et al. (2012). Super-Venus values were calculated in this study from simple interior models following Seager et al. (2007).

boundary temperatures were 2250, 2500, and 3000 K. In addition, five different values were tested for the amount of internal heating Q_0. Compositional buoyancy was set as $(d\rho/d\phi)$ = 120 kg m^{-3} for all simulations. The fraction of light elements in the core was fixed at 0.2 for all simulation runs to avoid inner core solidification (Schubert et al., 1992; Fraeman and Korenaga, 2010). Simulations were performed for all permutations of the above initial conditions, although unrealistic simulation results were discarded in the following way: For both Venus and Mars, inner core growth was disallowed and total surface heat flux at the present was required to be positive. Furthermore, the condition $h_c(t_p) < 500$ km was imposed to disregard results with unrealistic crust growth. None of the 675 simulations for Venus failed these criteria, but 30 of the 675 simulations for Mars were discarded.

The appropriate magnitude of radiogenic heating is poorly constrained in general, especially for terrestrial exoplanets. Even for Earth, the abundance of radiogenic heating is controversial. Geochemical constraints support a low Urey ratio, the ratio of internal heat production to surface heat flux, but this is known to conflict with the cooling history of Earth unless a non-classical heat-flow scaling for mantle convection is assumed (Christensen, 1985; Korenaga, 2008). A Urey ratio close to one has thus long been preferred from a geophysical perspective (Davies, 1980; Schubert et al., 1980, 2001) and can be used to provide an upper bound for the initial concentration of radioactive elements in Earth's chemically undifferentiated mantle. Assuming a present-day surface heat flux of 46 TW (Jaupart et al., 2007), an extreme upper bound for Earth is $Q_0 \approx 3.5\times10^{-7}$ W m^{-3}.

A recent petrological estimate on the thermal history of Earth is actually shown to

favor a low Urey ratio (∼0.3) with a non-classical heat-flow scaling (Herzberg et al., 2010), indicating that geochemical constraints on the heat budget may be robust. In the thermal evolution models of Kite et al. (2009), for example, concentrations of ^{40}K, ^{232}Th, ^{235}U, and ^{238}U taken from Ringwood (1991) and Turcotte and Schubert (2002) were considered, corresponding to values for Q_0 between 1.2×10^{-7} and 8.7×10^{-8} W m^{-3} for Venus. We thus chose to use the following values for initial volumetric radiogenic heating: Q_0 = 0.5, 0.75, 1.0, 1.25, and 1.75 $\times10^{-7}$ W m^{-3} (in the case of Venus). The default intermediate value is 1.0 $\times10^{-7}$ W m^{-3}. For other planets, Q_0 was multiplied by $\rho_m/\rho_{m,\varphi}$, where ♀ indicates the Venusian value, to maintain constant element abundances in more or less compressed mantles.

3.2 Application to super-Venus Planets

One-dimensional profiles of massive terrestrial exoplanets were generated to calculate planet-specific constants used in the above stagnant-lid convection model. Many interior structure models exist for massive solid exoplanets, ranging from simple to very complex (Valencia et al., 2006; Seager et al., 2007; Sotin et al., 2007; Wagner et al., 2011). To study the first-order effects of planetary mass on stagnant-lid convection, a relatively simple structure with an Fe(ϵ) core and a $MgSiO_3$ mantle is assumed, as in Seager et al. (2007) and Kite et al. (2009). The resulting interior density and pressure distributions neglect several obvious factors such as temperature effects, but yield results remarkably similar to those from more complex models.

Three equations are solved to calculate $m(r)$, the mass contained within radius r; $P(r)$, the pressure distribution; and $\rho(r)$, the density distribution. A self-consistent internal structure must satisfy the material specific equations of state

$$P(r) = f_{EOS}(\rho(r), T(r)), \tag{22}$$

the equation of hydrostatic equilibrium

$$\frac{dP(r)}{dr} = \frac{-Gm(r)\rho(r)}{r^2}, \tag{23}$$

and the conservation of mass equation for a spherical mass distribution

$$\frac{dm(r)}{dr} = 4\pi r^2 \rho(r), \tag{24}$$

where G is the gravitational constant; $T(r)$ is the radial temperature profile; and f_{EOS} represents a material-specific equation of state (Seager et al., 2007).

Equations of state are numerically calculated using constants from Table 3 to sufficient resolution so that $\rho(r)$ can be determined to within ± 1 kg m^{-3}. For a desired M_P, equations (23) and (24) are numerically integrated from the center of a planet with the inner boundary conditions $M(0) = 0$ and $P(0) = P_c$, where P_c is a guessed central pressure. The outer boundary condition is simply $P(R_P) = 0$. Temperature effects are ignored, since associated errors are limited to a few percent (Seager et al., 2007). With this method, the choice of P_c determines the R_P at which the outer boundary condition is satisfied. These calculations are iterated with the bisection method until P_c is found such that $m(R_P) = M_P$ to within 0.1%. The equation of state for Fe(ϵ) is used until $m(r) = 0.325 M_P$, mandating a 32.5% core mass fraction. The $MgSiO_3$ perovskite to enstatite phase transition is assumed to occur at 23 GPa (Sotin et al., 2007). Neglecting this phase transition would produce unrealistically high near-surface densities.

Material	K_0 (GPa)	$K_0^{'}$	$K_0^{''}$ (GPa^{-1})	ρ_0 (kg m^{-3})	EOS
Fe(ϵ)	156.2	6.08	N/A	8300	V
$MgSiO_3$(pv)	247	3.97	-0.016	4100	BME4
$MgSiO_3$(en)	125	5	N/A	3220	BME3

Table 3: Material constants used to generate interior structure models, taken from Seager et al. (2007). Using three different equations of state, $P(\rho)$ is calculated to high resolution for each material. The Vinet and 3rd and 4th order Birch-Murnaghan equations of state are abbreviated V, BME3, and BME4, respectively.

Pressure, mass, and density distributions were calculated for planets with $M_P = 1$, 2, 4, 5, 6, 8, and $10 M_\oplus$. From these models, averaged densities for the core and mantle were calculated, along with P_c and P_{cm}. Surface gravitational accelerations were calculated using $g = GM_P/R_P^2$ for each planet. These constants are reported in Table 2. The density distributions for these planets are shown in Fig. 2, along with the density profile for Earth from the Preliminary Reference Earth Model (PREM) of Dziewonski and Anderson (1981). Compared to PREM, the scheme for calculating internal structures used in this study overestimates the density of the core and underestimates the radius of the core of an Earth-mass planet, but returns $R_P(M_\oplus) \approx R_\oplus$ despite ignoring details of mineral composition, phase transitions, and temperature effects. In more massive planets, the enstatite to perovskite phase transition occurs at much shallower depths because a higher surface gravity causes a greater increase in pressure with depth. Furthermore, P_c increases

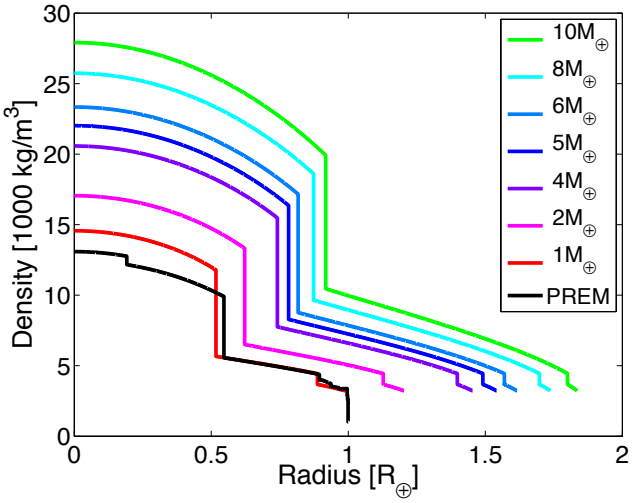

Figure 2: Interior density distributions for super-Venus planets with M_P = 1, 2, 4, 5, 6, 8, and $10M_\oplus$. The material equations of state and the equations of conservation of mass and hydrostatic equilibrium were numerically integrated to build simple planets, and the interior boundary condition was adjusted until the resulting planet had the desired mass. These simple models are used to calculate averaged values for mantle density, ρ_m; core density, ρ_c; surface gravity, g; central pressure, P_c; and core/mantle boundary pressure, P_{cm}. For comparison, the density distribution for Earth from the Preliminary Reference Earth Model (PREM) of Dziewonski and Anderson (1981) is also plotted.

much more rapidly than P_{cm} with increasing planetary mass.

Most of the Martian and Venusian initial conditions can be used for super-Venus thermal evolution models, but some must be modified appropriately. For example, the core/mantle temperature for super-Venus planets should increase along the mantle adiabatic temperature gradient: for 5 and $10M_\oplus$ super-Venus planets, initial core/mantle boundary temperatures are increased by roughly 350 and 900 K, respectively, from the initial conditions for Venus. These temperatures still correspond to a so-called "hot start," which is likely for terrestrial planets because of the large magnitude of gravitational potential energy released during accretion (Stevenson et al., 1983). Only three simulations for the $5M_\oplus$ planet, and no simulations for the $10M_\oplus$ planet, failed the requirements on crustal thickness, surface heat flux, and inner core growth.

4 Results

Thermal evolution simulations were performed for Mars, Venus, and super-Venus planets. The following sections summarize the results, beginning with a few representative examples for Mars and Venus. Then, principal component analysis was applied using all simulation results to identify major model behaviors. We also tried to quantify relations between input and output parameters, and despite the complexity of our model formulation, a linear function of initial conditions is found to reasonably approximate many output parameters of interest.

4.1 Sample thermal histories for Mars and Venus

Sample thermal histories for Mars and Venus are shown in Fig. 3. These models span the entire range of initial radiogenic heating values with all other initial conditions set to intermediate values. In particular, $T_u(0) = 1700$ K, $\mu_0 = 10^{19}$ Pa s, and $\Delta\mu_w = 100$. For Venus and Mars, respectively, $T_{cm}(0) = 4000$ and 2500 K and $T_s = 220$ and 730 K. Initially very hot cores are assumed here because core segregation is expected to release a large amount of gravitational potential energy. This excess heat is released into the mantle during the first hundred million years of planetary evolution. Thereafter, mantle dynamics controls core cooling. Whereas internal heating has a great effect on surface heat flux, mantle temperatures only differ to within $\pm$200 K for the sampled range of Q_0. Mars evolves with a consistently lower potential temperature than Venus. Because Mars also has a relatively shallow mantle, the Martian core is cooled down more efficiently.

Crustal thickness is an important, potentially observable constraint for planetary evolution models. Mars and Venus, with different magnitudes of radiogenic heating, have very different crustal formation histories. Both planets start with no initial crust, but quickly produce some through mantle melting. For Venus, Moho temperatures quickly reach the melting point of basalt for all initial internal heating choices. Crustal production occurs for the first $\sim$1 Gyr of evolution, with thicker crust for higher internal heating. For Mars, crustal production is gradual and crustal temperatures are much lower, with increased internal heating causing an longer period of crustal formation and increased total crustal production. Both Mars and Venus undergo substantial mantle processing, indicating that the deep interior serves as a significant source of endogenous water, especially during the first $\sim$1.5 Gyr of their evolution.

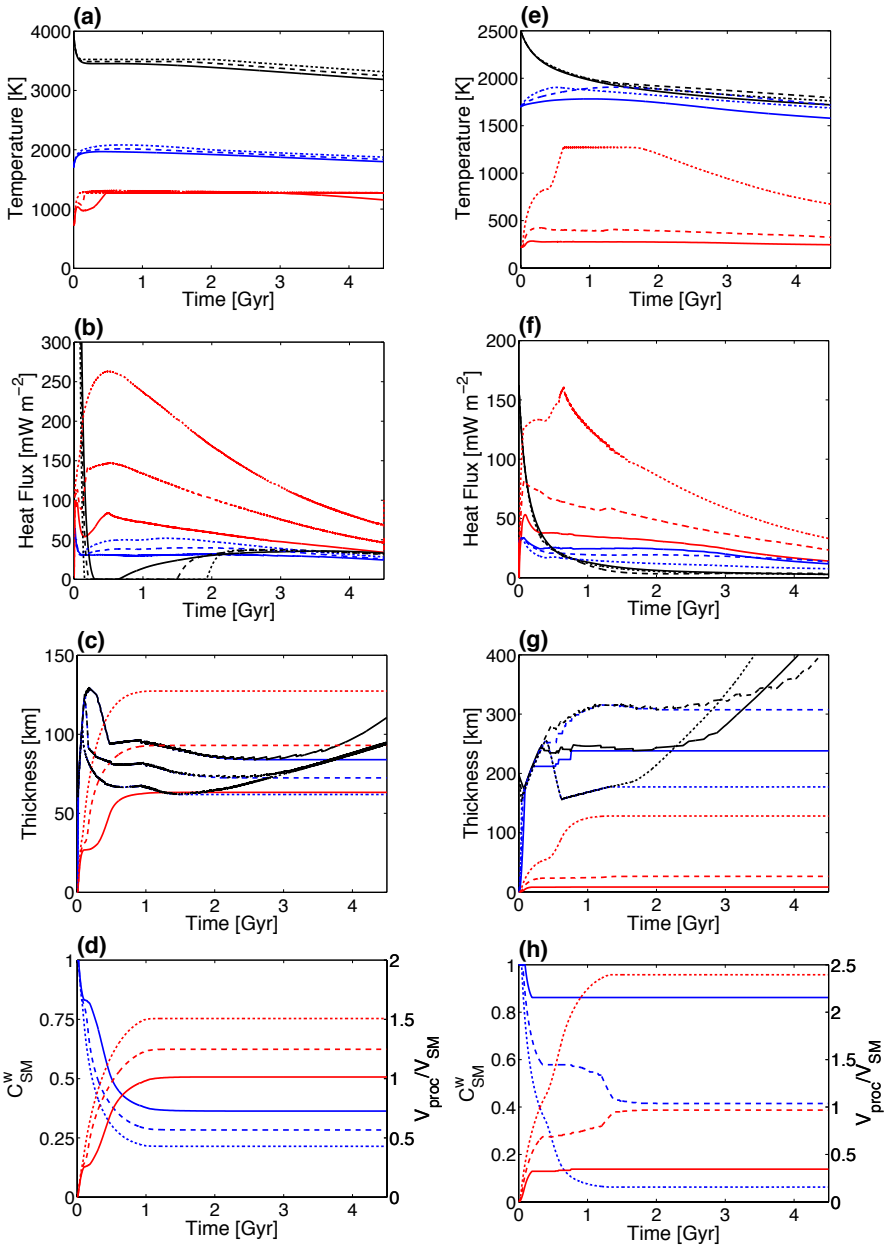

Figure 3: Sample histories for Venus (left) and Mars (right). From top to bottom, red curves signify Moho temperature, surface heat flow, crustal thickness, and normalized mantle water content. Likewise, blue curves represent mantle potential temperature, mantle heat flux, depleted mantle lithosphere thickness, and fraction of processed source mantle; green curves show core/mantle boundary temperature, core heat flux, and lithosphere thickness. Solid, dashed, and dotted lines indicate Venusian $Q_0 = 0.5$, 1.0, and 1.75 $\times 10^{-7}$ W m^{-3}, respectively. Default initial conditions are $T_u(0) = 1700$ K, $\eta_0 = 10^{19}$ Pa $\cdot$ s, $\Delta\eta_w = 100$, and $(d\rho/d\phi) = 120$ kg m^{-3}. Venus and Mars have $T_{cm}(0) = 4000$ and 2500 K, respectively. Because crustal melting causes highly discontinuous surface heat flux, a moving average with a 75 Myr span was used for plotting purposes.

4.2 Sensitivity analyses for the evolution of Mars and Venus

Figures 4 and 5 summarize the results of 1320 simulations for Venus and Mars, respectively. Present-day values for selected output parameters are plotted against crustal thickness for both planets. Several correlations are readily apparent. For Venus, thicker crust is associated with higher Moho temperature, more mantle processing, higher mantle heat flux, and quicker crustal formation. More specifically, Moho temperature increases with crustal thickness in a linear fashion until $h_c \approx 75$ km, after which Moho temperatures remain near the critical value for basalt melting. Simulations with crustal melting have highly discontinuous surface and mantle heat fluxes, but such discontinuous nature is merely an artifact owing to our particular numerical implementation, so average values of F_s and F_m over the final 100 Myr of planetary evolution are used for all subsequent analyses. In contrast, Moho temperatures for Mars only approach the critical value for basalt melting in simulations with the thickest crust. Unlike for Venus, a decrease in present-day mantle heat flux accompanies an increase in crustal thickness for Mars.

Principal component analysis facilitates the interpretation of the correlations between output parameters. For Venus, four principal components account for the vast majority ($\sim$90%) of the variance of the planetary parameters after 4.5 Gyr of thermal evolution. Principal components for Venus and Mars are reported in Table 4. Arrows representing the eigenvectors associated with these principal components are also plotted in Figs. 4 and 5. These arrows indicate the axes along which the vast majority of the variance in the model output primarily lies. No preferred polarity exists for the principal component eigenvectors; plotting these arrows with a 180° rotation would be equally valid.

The first principal component represents the most dominant correlations among present-day planetary parameters, which are characterized mainly by the thicknesses of the crust and mantle lithosphere layers, as they are associated with large coefficients: h_c (0.34), h_l (-0.36), and h_{ML} (-0.39). Because the sign of the coefficient for h_c is opposite to the sign of the other two coefficients, the thicknesses of the crust and mantle lithosphere are anti-correlated. In other words, thick crust is associated with thin depleted mantle lithosphere and a thin thermal boundary layer and vice versa, since principal components have no preferred polarity. Other coefficients in the first principal component indicate the effects of crustal thickness on other model parameters, including the first-order correlations observed during inspection of Fig. 4. For instance, thick crust is associated with high Moho temperature and high surface and mantle heat fluxes. Thick crust also indicates a high degree of mantle processing and a corresponding low present-day mantle water content. Finally, the

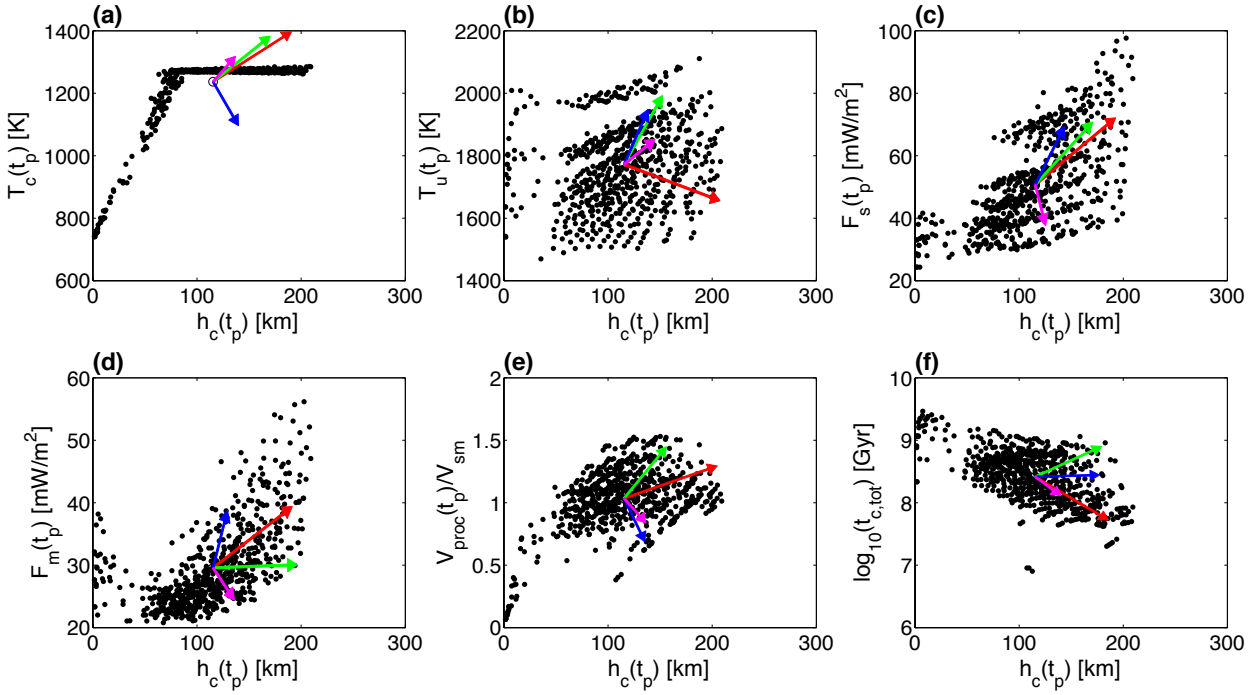

Figure 4: Summary of parameter values at the present for 675 simulations of the thermal evolution of Venus. Arrows are projections of the principal component basis vectors that emanate from a point representing the averaged simulation results, indicating axes that account for the vast majority of the data set's variance. The percentage of cumulative variance represented by each arrow's principal component decreases with arrow length. From greatest to least represented variance, arrow colors are red, green, blue, and magenta. Panels show (a) Moho temperature, (b) mantle potential temperature, (c) surface heat flux, (d) mantle heat flux, (e) fraction of mantle processed by melting, and (f) total time for crust to grow from 10% to 95% of its present thickness as functions of crustal thickness. Because crustal melting causes highly discontinuous surface and mantle heat fluxes, the model outputs are the averaged values for the final 100 Myr of planetary evolution.

large negative coefficients for both $t_{c,10\%}$ and $\log_{10}(\Delta t_{c,tot})$ indicate that thick crust tends to form early and quickly.

The remaining principle components represent additional aspects of the evolution of Venus. For instance, the second principal component elucidates the effects of planet temperatures on other model parameters because large coefficients are associated with T_u (0.45) and T_{cm} (0.44). Unsurprisingly, high mantle potential and core/mantle boundary temperatures are associated with high Moho temperature, since T_c has a coefficient of 0.25. Moreover, high interior temperatures correspond to thick crust and a high degree of mantle processing, which would cause the present-day mantle water concentration to be very low.

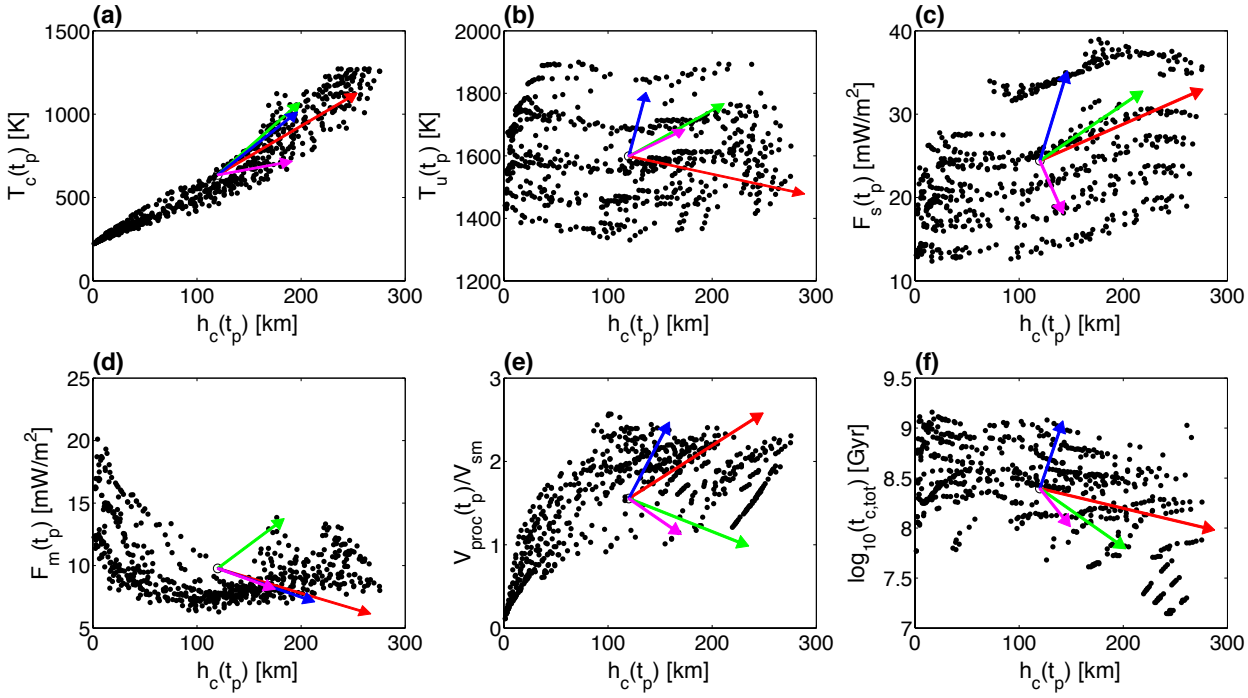

Figure 5: Summary of parameter values at the present for 645 simulations of the thermal evolution of Mars. Arrows are projections of the principal component basis vectors that emanate from a point representing the averaged simulation results, indicating axes that account for the vast majority of the data set's variance. The percentage of cumulative variance represented by each arrow's principal component decreases with arrow length. From greatest to least represented variance, arrow colors are red, green, blue, and magenta. Panels show (a) Moho temperature, (b) mantle potential temperature, (c) surface heat flux, (d) mantle heat flux, (e) fraction of mantle processed by melting, and (f) total time for crust to grow from 10% to 95% of its present thickness as functions of crustal thickness. Because crustal melting causes highly discontinuous surface and mantle heat fluxes, the model outputs are the averaged values for the final 100 Myr of planetary evolution.

Note, however, that high interior temperatures do not correspond to thick crust in case of the first principal component (Fig. 4b). In this space of crustal thickness and upper mantle temperature, the first and second principal components are nearly orthogonal, thus explaining the overall spread of simulation results. With principal component analysis, we can visualize how the most dominant trend (represented by the first principal component) is affected by secondary factors and how these secondary factors manifest in different parameter spaces. An important point is that the overall variability of planetary evolution can be compactly represented by just four principal components; that is, the effective dimension of the model space is only four.

Parameter	V1	V2	V3	V4	Av.	SD	M1	M2	M3	M4	Av.	SD
T_c [K]	0.29	0.25	-0.26	0.20	1237	106	0.35	0.30	0.09	0.05	636	307
T_u [K]	-0.14	0.45	0.28	0.11	1772	132	-0.16	0.23	0.50	0.17	1599	132
T_{cm} [K]	-0.10	0.44	0.30	0.23	3128	215	-0.15	0.23	0.47	0.26	1752	53.7
h_c [km]	0.34	0.23	0.11	0.13	115	43.1	0.37	0.21	0.07	0.18	120	78.6
h_l [km]	-0.36	0.20	0.21	0.02	53.6	29.1	-0.35	0.10	0.32	0.13	160	84.2
h_{ML} [km]	-0.39	0.20	0.07	0.03	84.1	27.7	-0.16	-0.50	0.14	0.13	423	133
F_s [mW m^{-2}]	0.28	0.24	0.22	-0.50	50.7	14.7	0.23	0.20	0.31	-0.58	24.4	7.04
F_m [mW m^{-2}]	0.29	0.01	0.49	-0.22	29.6	6.58	-0.28	0.40	-0.06	-0.17	9.77	2.60
$\log_{10}(u)$	0.28	-0.17	0.41	-0.06	0.89	0.26	-0.12	0.43	-0.26	-0.23	0.10	0.16
C_{sm}^w	-0.19	-0.36	0.37	0.13	0.37	0.13	-0.38	0.13	-0.20	0.06	0.27	0.25
V_{proc}/V_{sm}	0.17	0.39	-0.33	-0.21	1.04	0.25	0.38	-0.13	0.20	-0.20	1.55	0.62
$t_{c,10\%}$ [Gyr]	-0.26	-0.04	-0.08	-0.70	0.12	0.23	-0.29	-0.05	-0.07	-0.44	0.17	0.24
$\log_{10}(\Delta t_{c,tot})$	-0.34	0.18	0.01	-0.16	8.42	0.42	-0.17	-0.28	0.37	-0.43	8.40	0.44
$\lambda_i/\Sigma\lambda_i$	0.41	0.27	0.16	0.06	-	-	0.42	0.23	0.19	0.07	-	-

Table 4: Principal component basis matrix for Venus (V) and Mars (M) for the model output after 4.5 Gyr of planetary evolution. Four eigenvectors account for over 85% of the variance in the normalized and mean subtracted simulation results. The fractions of the cumulative variances for which each principal component accounts, calculated by dividing the principal component eigenvalue by the sum of the eigenvalues for all principal components, are in the bottom row. Output parameters were mean subtracted and normalized using the listed average and standard deviation values.

The principal components for Mars are very similar to those for Venus, with some notable exceptions. The first principal component again represents the effects of strongly correlated Moho temperature and crustal thickness, and thus explains the largest portion of the variance in the model output. As for Venus, a thin, cold crust is associated with thick depleted mantle lithosphere, a thick thermal boundary layer, a low surface heat flux, and a low degree of mantle processing. Unlike Venus, however, the surface and mantle heat fluxes in the first principal component are anti-correlated (see also Fig. 5).

Despite the complexity of our thermal evolution model, some present-day parameters are found to be predicted with reasonable accuracy for Venus and Mars using a linear function. A general formula for this function is

$$B_i = A_{i,0} + A_{i,1}T_{u,n}(0) + A_{i,2}T_{cm,n}(0) + A_{i,3}(\log_{10}(\eta_0))_n + A_{i,4}(\log_{10}(\Delta\eta_w))_n + A_{i,5}Q_{0,n}, \quad (25)$$

where B_i is the value of the desired output parameter after 4.5 Gyr, constants $A_{i,0}$ through $A_{i,5}$ are estimated using the least-squares method for each B_i, and the subscript n indicates that the input parameters are normalized and mean subtracted.

B_i	$A_{i,0}$	$A_{i,1}$	$A_{i,2}$	$A_{i,3}$	$A_{i,4}$	$A_{i,5}$	Units	Corr.
T_u	1772	43.6	11.3	89.9	69.4	30.4	K	0.95
T_{cm}	3128	88.5	32.5	137.0	104.8	48.8	K	0.94
h_c	115	26.4	22.2	-2.98	-7.84	18.0	km	0.92
h_l	53.6	-2.17	-5.51	17.5	17.8	-6.07	km	0.91
h_{ML}	84.1	-4.82	-4.87	19.2	14.9	-6.87	km	0.94
F_s	50.7	3.96	2.38	-1.87	-0.76	13.5	mW m^{-3}	0.98
F_m	29.6	3.40	1.51	-1.91	-1.55	2.92	mW m^{-3}	0.81
$\log_{10}(u)$	0.89	0.11	0.01	-0.15	-0.07	0.04	-	0.82
V_{proc}/V_{sm}	1.04	0.00	0.06	-0.01	0.07	0.16	-	0.74
$\log_{10}(\Delta t_{c,tot})$	8.42	-0.15	-0.16	0.22	0.20	0.01	-	0.87

Table 5: Coefficients for the best-fit linear function (Eq. 25) relating parameter values after 4.5 Gyr for parameters with correlation coefficients > 0.70 to a given set of initial conditions for Venus. Correlation coefficients quantifying the correspondence between the actual and predicted output parameters were calculated using normalized and mean subtracted input and output parameters. The average values of the input parameters are $T_u(0) = 1700$ K, $T_{cm}(0) = 4000$ K, $\log_{10}(\eta_0) = 19$, $\log_{10}(\Delta\eta_w) = 1$, and $Q_0 = 1.05 \times 10^{-7}$ W m^{-3}. For the best-fit function, the input parameters are mean subtracted and normalized by 212 K, 408 K, 0.82, 0.82, and 4.30×10^{-8} W m^{-3}, respectively.

Table 5 lists constants for Venusian B_i that have relatively high correlation coefficients between predicted and actual simulation results. Figure 6 shows contour plots with predicted values of mantle potential temperature, crustal thickness, and duration of crustal formation for given initial internal heating and mantle potential temperature. While present-day mantle potential temperature and crustal thickness depend strongly on both initial mantle potential temperature and the magnitude of internal heating, the total duration of crustal formation is primarily a function of initial mantle potential temperature (see Table 5 for more complete information on parameter sensitivity). Figure 6 also demonstrates a reasonable correspondence between the predicted and actual values of these model outputs for all of the simulations. This way of summarizing simulation results allows us not only to see the sensitivity of model outputs to initial parameters but also to quickly reproduce major modeling results without redoing simulation.

4.3 Evolution of super-Venus planets

We investigate the evolution of super-Venus planets to explore the effects of planetary mass on stagnant-lid convection. For simplicity, surface temperatures for all super-Venus planets are assumed to be 300 K, though in reality this temperature may vary with time and is

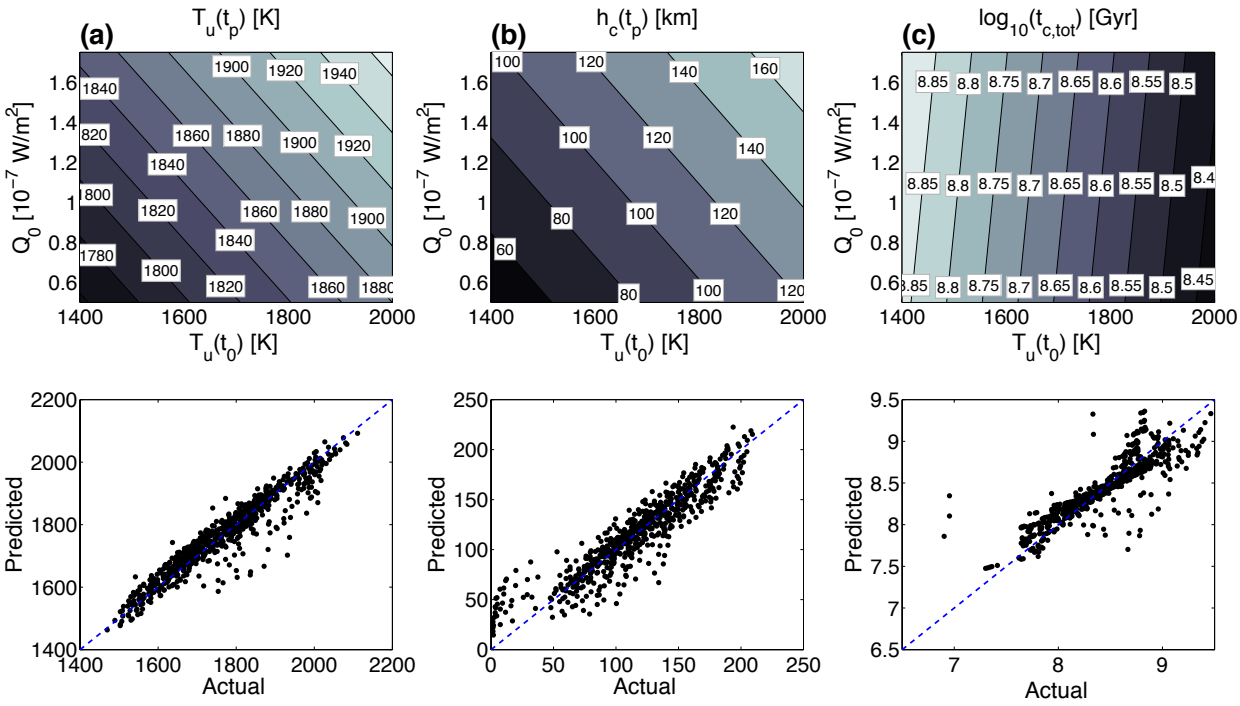

Figure 6: Top panels show predicted values for Venus after 4.5 Gyr given initial volumetric radiogenic heating and initial mantle potential temperature, the initial conditions to which the output is most sensitive. Bottom panels show the correspondence between predicted and actual simulation results. The dashed line represents perfect predictive power. Default initial conditions are $T_{cm}(0) = 4000$ K, $\eta_0 = 10^{19}$ Pa $\cdot$ s, $\Delta\eta_w = 100$, and $(d\rho/d\phi) = 120$ kg m^{-3}. Panels show predicted values of (a) mantle potential temperature, (b) crustal thickness, and (c) total time for crust to grow from 10% to 95% of its present thickness.

highly dependent on atmospheric composition.

4.3.1 Sample thermal histories

Super-Venus planets with $M_P = 1$, 5, and $10M_\oplus$ were evolved to study the effects of increasing planetary mass on a variety of parameters, particularly crustal production. For all three planets, Q_0 was scaled to the Venusian value of 1.0×10^{-7} W m^{-3}, $T_u(0) = 1700$ K, and $T_{cm}(0) = 4000$, 4350, and 4900 K, respectively. Dehydration stiffening and compositional buoyancy were both incorporated as usual. Figure 7 shows the results of these simulations. As with Venus and Mars, the transient "hot start" in the core is lost in the first $\sim$100 Myr. After this initial cooling, mantle dynamics controls core cooling. Because the mantle heats up for the first $\sim$1 Gyr and then cools only very slowly, core cooling is precluded for the first $\sim$2 Gyr. As suggested by simple scaling laws (Stevenson, 2003),

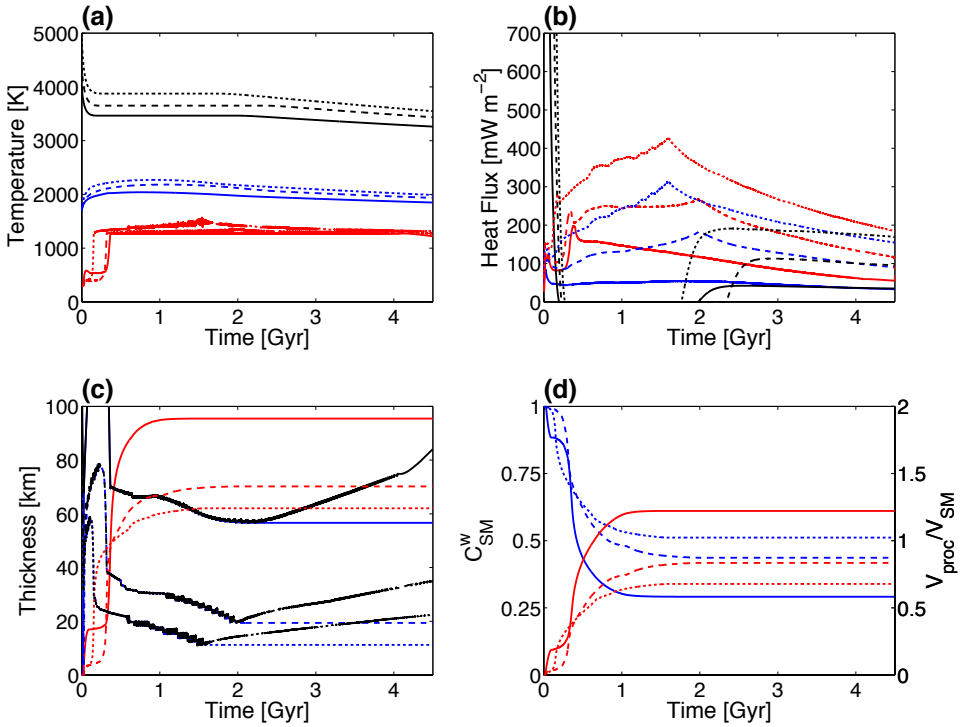

Figure 7: Sample histories for $1M_\oplus$ (solid lines), $5M_\oplus$ (dashed lines), and $10M_\oplus$ (dotted lines) super-Venus planets. Red, blue, and black curves, respectively, signify (a) crust, mantle potential, and core/mantle boundary temperatures, (b) surface, mantle, and core heat flows, (c) crust, depleted mantle lithosphere, and mantle lithosphere thicknesses, and (d) normalized mantle water content and fraction of processed source mantle. Default initial conditions are $Q_0 = 1.0 \times 10^{-7}$ W m^{-3} (scaled with ρ_m), $T_u(0) = 1700$ K, $\eta_0 = 10^{19}$ Pa $\cdot$ s, $\Delta\eta_w = 100$, and $(d\rho/d\phi) = 120$ kg m^{-3}. The 1, 5, and $10M_\oplus$ planets have $T_{cm}(0) =$ 4000, 4350, and 4900 K, respectively. Because crustal melting causes highly discontinuous surface and mantle heat fluxes, a moving average with a 75 Myr span was used for plotting purposes.

mantle cooling paths for massive super-Venus planets are roughly parallel.

Figure 7 also shows how the thicknesses of the crust, mantle lithosphere, and depleted mantle lithosphere vary with time. With increasing planetary mass, crustal thickness decreases. The simple scaling analyses below indicate that more massive planets have greater melt production. The observed increase in mantle potential temperature with planetary mass only accentuates this effect. The increased melt volume, however, is not sufficient to create a thicker crust on a larger planet. The $1M_\oplus$ planet in the stagnant-lid regime ceases crustal production soon after 1 Gyr as mantle potential temperature drops below a critical value. The increased interior temperatures for the more massive planets allow longer dura-

tions of crustal production. For the first ∼2 Gyr of thermal evolution, the thickness of the depleted mantle lithosphere is close to that of the mantle thermal lithosphere, reflecting the continuous delimitation of excess depleted mantle lithosphere. Decreased crustal production with increasing planetary mass corresponds to a smaller degree of mantle processing and a higher content of residual mantle water.

4.3.2 Sensitivity analyses

The output of 1347 simulations for 5 and $10M_{\oplus}$ super-Venus planets are shown in Figs. 8 and 9. Three simulations for the $5M_{\oplus}$ super-Venus planet were excluded because they did not meet the requirements that $h_c < 500$ km and that inner core growth did not occur. As for Mars and Venus, present-day parameters of interest are plotted against present-day crustal thickness. The principal component eigenvectors, explained below, are projected onto each plot, emanating from the average simulation output.

These scatter plots reveal similarities between the evolution of both massive planets. For instance, Moho temperature increases with crustal thickness in a linear fashion before reaching the critical value for basalt melting. With increasing planetary mass, the critical crustal thickness at which this transition occurs decreases. For relatively thick crust, Moho temperatures remain near the critical value for basalt melting. For both super-Venus planets, an increase in crustal thickness is associated with an increase in present-day mantle potential temperature, mantle heat flux, and degree of mantle processing. The total duration of crustal formation decreases with increasing present-day crustal thickness. Again, correlations between model parameters may be studied in more detail with principal component analysis.

Table 6 lists dominant principal components for 5 and $10M_{\oplus}$ super-Venus planets, which are almost identical. For both planets, as for Venus and Mars, the first principal component is characterized by a strong correlation between Moho temperature and crustal thickness, explaining the general trends observed in Figs. 8 and 9. A decrease in both quantities is associated with an increase in the thicknesses of the depleted mantle lithosphere and the thermal boundary layer, a decrease in surface and mantle heat fluxes, an increase in the duration of crustal formation, and a decrease in the degree of mantle processing. The second principal component illuminates the effect of correlated interior temperatures. As expected, increasing mantle potential and core/mantle boundary temperatures causes an increases in crustal thickness, the total duration of crustal formation, and the degree of mantle processing. The third principal component details the effect of anti-correlated Moho and

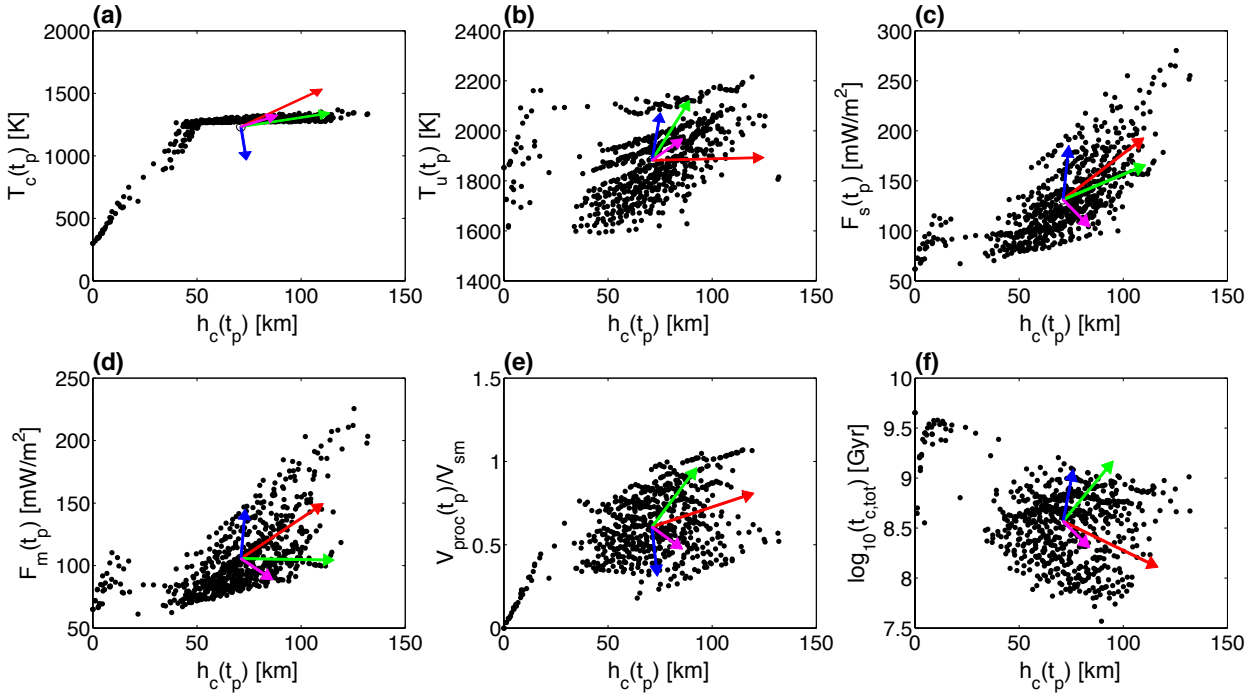

Figure 8: Summary of parameter values at the present for 672 simulations of the thermal evolution of a $5M_{\oplus}$ super-Venus. Arrows are projections of the principal component basis vectors that emanate from a point representing the averaged simulation results, indicating axes that account for the vast majority of the data set's variance. The percentage of cumulative variance represented by each arrow's principal component decreases with arrow length. From greatest to least represented variance, arrow colors are red, green, blue, and magenta. Panels show (a) Moho temperature, (b) mantle potential temperature, (c) surface heat flux, (d) mantle heat flux, (e) fraction of mantle processed by melting, and (f) total time for crust to grow from 10% to 95% of its present thickness as functions of crustal thickness. Because crustal melting causes highly discontinuous surface and mantle heat fluxes, the model output is the averaged values for the final 100 Myr of planetary evolution.

interior temperatures. If present-day interior temperatures are increased while the Moho temperate is decreased, the thickness of the mantle lithosphere layers would increase, along with surface and mantle heat fluxes. Convective velocities would also increase, but the degree of mantle processing would remain low.

Many present-day model parameters of interest can be represented as a linear function of initial conditions (Table 7). Compared to the case of Venus, a greater number of parameters are found to be approximated reasonably well by this approach. The effects of melting at the base of the crust undoubtedly remain a large source of nonlinearity in the model output for

Parameter	F1	F2	F3	F4	Av.	SD	T1	T2	T3	T4	Av.	SD
T_c [K]	0.35	0.07	-0.32	0.16	1233	190	0.36	0.03	-0.23	0.26	1309	112
T_u [K]	0.01	0.47	0.21	0.25	1882	137	0.03	0.45	0.28	0.25	1948	138
T_{cm} [K]	0.06	0.45	0.24	0.37	3331	214	0.06	0.43	0.31	0.28	3475	225
h_c [km]	0.37	0.21	0.03	0.25	71.1	23.4	0.34	0.22	0.11	0.32	63.0	16.6
h_l [km]	-0.33	0.20	0.26	-0.02	17.5	11.5	-0.34	0.17	0.33	-0.20	11.1	5.83
h_{ML} [km]	-0.38	0.18	0.14	0.10	32.0	13.2	-0.37	0.21	0.16	0.14	20.7	6.89
F_s [mW m^{-2}]	0.35	0.11	0.30	-0.32	131	38.7	0.37	0.14	0.17	-0.33	204	61.6
F_m [mW m^{-2}]	0.34	-0.00	0.41	-0.23	106	28.2	0.37	0.07	0.26	-0.31	173	46.7
$\log_{10}(u)$	0.26	-0.19	0.42	-0.24	1.65	0.28	0.30	-0.14	0.32	-0.40	2.00	0.30
C^w_{sm}	-0.19	-0.36	0.36	0.24	0.57	0.12	-0.12	-0.36	0.46	0.14	0.62	0.10
V_{proc}/V_{sm}	0.17	0.38	-0.33	-0.25	0.61	0.21	0.12	0.38	-0.44	-0.14	0.50	0.16
$t_{c,10\%}$ [Gyr]	-0.25	0.17	-0.14	-0.51	0.20	0.29	-0.27	0.19	-0.14	-0.30	0.13	0.21
$\log_{10}(\Delta t_{c,tot})$	-0.23	0.33	0.17	-0.32	8.57	0.37	-0.18	0.36	-0.01	-0.38	8.54	0.38
$\lambda_i/\Sigma\lambda_i$	0.41	0.28	0.15	0.06	-	-	0.42	0.30	0.12	0.07	-	-

Table 6: Principal component basis matrix for $5M_\oplus$ (F) and $10M_\oplus$ (T) super-Venus planets for the model output after 4.5 Gyr of planetary evolution. Four eigenvectors account for roughly 90% of the variance in the normalized and mean subtracted simulation results. The fractions of the cumulative variances for which each principal component accounts, calculated by dividing the principal component eigenvalue by the sum of the eigenvalues for all principal components, are in the bottom row. Output parameters were mean subtracted and normalized using the listed average and standard deviation values.

B_i	$A_{i,0}$	$A_{i,1}$	$A_{i,2}$	$A_{i,3}$	$A_{i,4}$	$A_{i,5}$	Units	Corr.
T_u	1882	42.1	13.6	93.9	57.7	46.6	K	0.92
T_{cm}	3331	94.1	41.7	132.2	79.0	74.7	K	0.92
h_c	71.1	12.4	8.31	1.47	-0.64	14.6	km	0.89
h_l	17.5	-1.31	-1.71	5.35	4.87	-3.97	km	0.74
h_{ML}	32.0	-2.89	-2.42	7.57	5.00	-5.08	km	0.84
F_s	131.1	12.9	7.56	-8.81	-4.12	32.1	mW m^{-3}	0.95
F_m	105.6	11.8	6.57	-9.08	-6.87	17.7	mW m^{-3}	0.89
$\log_{10}(u)$	1.65	0.10	0.03	-0.18	-0.07	0.07	-	0.84
C^w_{sm}	0.57	0.00	-0.01	-0.01	-0.06	-0.07	-	0.78
V_{proc}/V_{sm}	0.61	0.00	0.02	0.02	0.11	0.13	-	0.83
$t_{c,10\%}$	0.20	-0.15	-0.10	0.10	0.08	-0.03	Gyr	0.76
$\log_{10}(\Delta t_{c,tot})$	8.57	-0.09	-0.12	0.17	0.19	0.03	-	0.79

Table 7: Coefficients for the best-fit linear function (Eq. 25) relating parameter values after 4.5 Gyr for parameters with correlation coefficients > 0.70 to a given set of initial conditions for a $5M_\oplus$ super-Venus. Correlation coefficients quantifying the correspondence between the actual and predicted output parameters were calculated using normalized and mean subtracted input and output parameters. The average values of the input parameters are $T_u(0) = 1701$ K, $T_{cm}(0) = 4351$ K, $\log_{10}(\eta_0) = 19$, $\log_{10}(\Delta\eta_w) = 1$, and $Q_0 = 1.73 \times 10^{-7}$ W m^{-3}. For the best-fit function, the input parameters are mean subtracted and normalized by 212 K, 408 K, 0.82, 0.82, and 7.07×10^{-8} W m^{-3}, respectively.

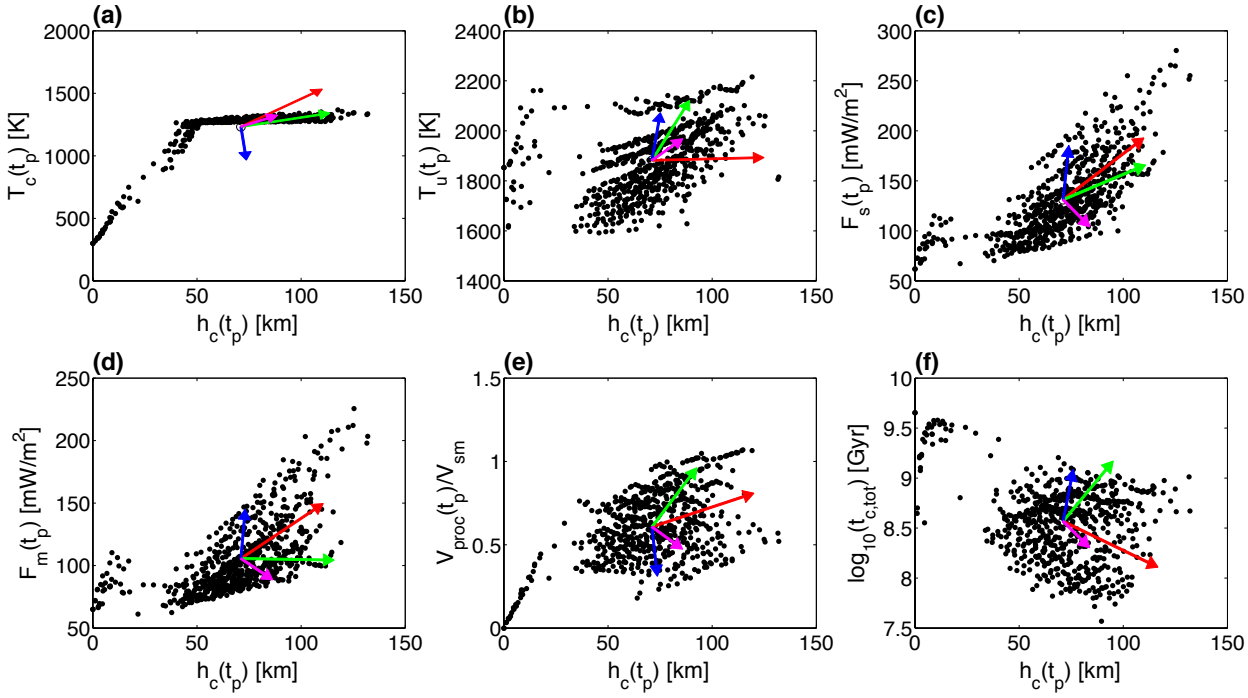

Figure 9: Summary of parameter values at the present for 675 simulations of the thermal evolution of a $10M_{\oplus}$ super-Venus. Arrows are projections of the principal component basis vectors that emanate from a point representing the averaged simulation results, indicating axes that account for the vast majority of the data set's variance. The percentage of cumulative variance represented by each arrow's principal component decreases with arrow length. From greatest to least represented variance, arrow colors are red, green, blue, and magenta. Panels show (a) Moho temperature, (b) mantle potential temperature, (c) surface heat flux, (d) mantle heat flux, (e) fraction of mantle processed by melting, and (f) total time for crust to grow from 10% to 95% of its present thickness as functions of crustal thickness. Because crustal melting causes highly discontinuous surface and mantle heat fluxes, the model output is the averaged values for the final 100 Myr of planetary evolution.

all terrestrial planets more massive than Mars. A more elaborate numerical implementation to deal with exceedingly high crustal temperatures may reduce such nonlinearity, though we did not explore this possibility.

4.4 Scaling of crustal thickness and mantle processing

We conduct simple scaling analyses to better understand the cause of decreasing crustal thickness and a decreasing degree of mantle processing with increasing planetary mass.

4.4.1 Crustal thickness

A number of parameters govern the scaling of crustal thickness with planetary mass. Increased melt production, for instance, is the first requirement for thicker crust. From Eq. 12, volumetric melt production for a planet may scale as

$$\frac{f_m}{f_{m,\oplus}} = \left(\frac{d_m}{d_{m,\oplus}}\right)\left(\frac{u}{u_\oplus}\right)\left(\frac{\phi}{\phi_\oplus}\right)\left(\frac{h_{m,\oplus}}{h_m}\right)\left(\frac{A_m}{A_{m,\oplus}}\right) \approx \left(\frac{M}{M_\oplus}\right)^{\delta}, \tag{26}$$

where the subscript $\oplus$ denotes values for an Earth-mass planet and A_m stands for the mantle surface area.

We can approximate δ using the representative interior models of Valencia et al. (2006), for which $R \propto M^{0.262}$, $\rho_m \propto M^{0.196}$, and $g \propto M^{0.503}$. First, consider the thickness of a melting region, $d_m = z_i$ - z_f. Since $z_f = P_f/(\rho_L g)$ is approximately constant for any planet,

$$\frac{d_m}{d_{m,\oplus}} \approx \frac{g_\oplus}{g} = \left(\frac{M}{M_\oplus}\right)^{-0.503}, \tag{27}$$

where a roughly constant mantle to core thickness ratio is assumed, although planetary mantles grow slightly more than cores with increasing planetary mass. Next,

$$\frac{u}{u_\oplus} = \frac{h_{m,\oplus}}{h_m}\left(\frac{Ra}{Ra_\oplus}\right)^{\frac{1}{2}}. \tag{28}$$

The Rayleigh number for a massive planet scales as

$$\frac{Ra}{Ra_\oplus} = \left(\frac{\Delta T_u}{\Delta T_{u,\oplus}}\right)\left(\frac{\eta(T_u)}{\eta(T_{u,\oplus})}\right)\left(\frac{g}{g_\oplus}\right)\left(\frac{\rho}{\rho_\oplus}\right)\left(\frac{h_m}{h_{m,\oplus}}\right)^3. \tag{29}$$

Assuming that the first and second terms on the right hand side are roughly equal to unity, we have

$$\frac{Ra}{Ra_\oplus} \approx \left(\frac{M}{M_\oplus}\right)^{1.485} \tag{30}$$

and thus

$$\frac{u}{u_\oplus} \approx \left(\frac{M}{M_\oplus}\right)^{0.481}. \tag{31}$$

Because h_c is usually much smaller than R_P,

$$\frac{A_m}{A_{m,\oplus}} = \left(\frac{R_P - h_c}{R_{P,\oplus} - h_{c,\oplus}}\right)^2 \approx \left(\frac{R_P}{R_{P,\oplus}}\right)^2 = \left(\frac{M}{M_\oplus}\right)^{0.524}. \tag{32}$$

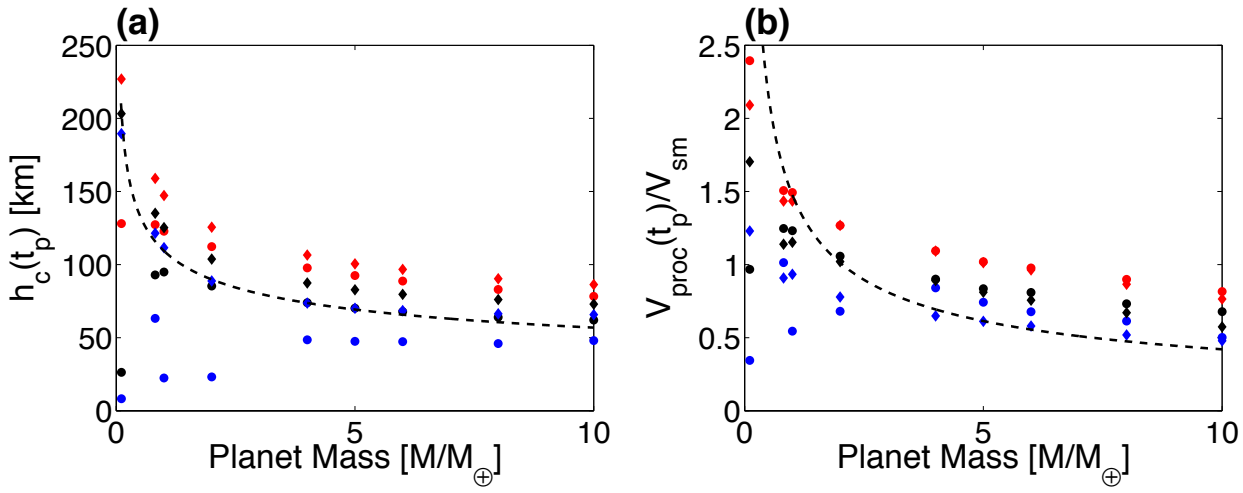

Figure 10: Summary of 54 simulations of the evolution of Mars, Venus, and seven super-Venus planets, showing the correspondence between simulation results and simple scaling laws for the effects of planetary mass on (a) crustal thickness and (b) mantle processing. Circles and triangles represent $T_u(0) = 1700$ and 2000 K, respectively. Blue, black, and red symbols represent Venus-equivalent $Q_0 = 5.0 \times 10^{-8}$, 1.0×10^{-7}, and 1.75×10^{-7} W m^{-3}, respectively. Dashed black lines show the scaling relations (a) $h_c \propto (M/M_\oplus)^{-0.284}$ and (b) $[(V_{proc}/V)/(V_{proc,\oplus}/V_\oplus)] \propto (M/M_\oplus)^{-0.546}$, with each curve fixed to intersect the average output from the simulations for the $2M_\oplus$ super-Venus planet.

Finally, the rest of the scaling relations may simply be assumed as

$$\frac{\phi}{\phi_\oplus} \approx 1 \tag{33}$$

and

$$\frac{h_{m,\oplus}}{h_m} \approx \left(\frac{M}{M_\oplus}\right)^{-0.262} . \tag{34}$$

Hence, $\delta \approx 0.240$ and $(f_m/f_{m,\oplus}) \approx (M/M_\oplus)^{0.240}$. Because $h_c \approx f_m \times \Delta t/(4\pi R_P^2)$, where Δt is the duration of crust growth, an increase in melt productivity with mass does not guarantee an increase in crustal thickness with mass. As planetary mass, and thus radius, increases, a larger volumetric melt production is required to produce a certain crustal thickness. Specifically, crustal thickness would only increase with mass for $\delta > 0.524$, assuming that Δt is roughly constant. Therefore, although melt productivity increases with planetary mass, this simple scaling analysis indicates that crustal thickness should decrease with scaling $(h_c/h_{c,\oplus}) \approx (M/M_\oplus)^{(0.240-0.524)} = (M/M_\oplus)^{-0.284}$.

Panel (a) of Fig. 10 is a plot of model output present-day crustal thickness as a function

of planetary mass for simulations of Mars, Venus, and seven super-Venus planets. While initial conditions strongly affect simulation results, the model outputs generally follow this simple scaling. Smaller planets can have thicker crust though they tend to be characterized by lower mantle temperatures.

4.4.2 Mantle processing

The scaling of mantle processing with planetary mass follows easily from the above analysis. A simplified equation for the volume of processed mantle is

$$V_{proc} \approx \frac{f_m}{\phi} \Delta t, \tag{35}$$

where Δt is a duration for crust growth.

Thus, the amount of processed mantle scales with planetary mass as

$$\frac{V_{proc}}{V_{proc,\oplus}} \approx \left(\frac{f_m}{f_{m,\oplus}} \right) \left(\frac{\phi_\oplus}{\phi} \right) \approx \left(\frac{M}{M_\oplus} \right)^\xi, \tag{36}$$

so $\xi \approx \delta \approx 0.240$.

The volume of a super-Venus planet scales as

$$\frac{V}{V_\oplus} = \left(\frac{R}{R_\oplus} \right)^3 \approx \left(\frac{M}{M_\oplus} \right)^\zeta, \tag{37}$$

so $\zeta = 0.786$. Therefore, $[(V_{proc}/V)/(V_{proc,\oplus}/V_\oplus)] \propto (M/M_\oplus)^{-0.546}$. Although the amount of processed mantle material increases with planetary mass, the fraction of processed mantle decreases with increasing planetary mass because the mantle volume increases more rapidly than the amount of processed material. Panel (b) in Fig. 10 confirms that the fraction of processed mantle does indeed decrease with increasing planetary mass according to this scaling law, although initial conditions strongly affect the simulation results.

4.5 Viscosity contrasts during stagnant-lid convection

Viscosity contrast across the lithosphere is tracked during each thermal evolution model, along with the critical viscosity contrast above which a planet is locked in the stagnant-lid regime. Figure 11 shows the output of 595 simulations for Mars, Venus, and two super-Venus planets for which Q_0, $T_u(0)$, and μ were varied over a wide range. In particular, all

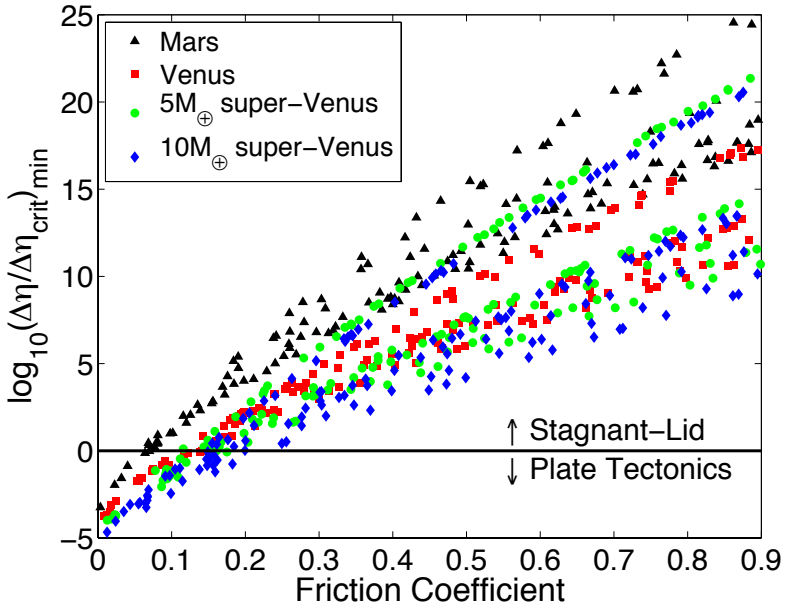

Figure 11: Summary of 595 simulations of the evolution of Mars, Venus, and two super-Venus planets, showing the minimum ratio of actual viscosity contrast to critical viscosity contrast and thus the likelihood of plate tectonics being favored at some point during 4.5 Gyr of planetary evolution. Each planet was evolved from six different sets of initial conditions (three values for both radiogenic heating and mantle potential temperature) for many different values of μ, the effective friction coefficient. Points plotted above the indicated line represent simulations for which the actual viscosity contrast never dipped below the critical value for a transition to plate tectonics. Below the indicated line, which occurs only for $\mu < 0.3$, plate tectonics may have been favored at some point. For dry silicate rocks, $\mu \sim 0.7$ to 0.8.

permutations of $Q_0 = 0.5$, 1.0, and 1.75 $\times 10^{-7}$ W m^{-3} (scaled as usual with ρ_m) and $T_u(0)$ = 1400, 1700, and 2000 K were considered for a range of μ between 0.0 and 0.9.

From this plot, several conclusions may be drawn. First, for values of the frictional coefficient associated with dry silicate rocks, $\mu \sim 0.7$ to 0.8, plate tectonics is never favored. Second, increasing planetary mass does not substantially affect the likelihood of plate tectonics. Third, the effects of choosing different initial conditions are amplified for greater planetary mass. Finally, although choosing extreme initial conditions can change the viscosity contrast by orders of magnitude, the effect of the friction coefficient is far more important.

5 Discussion

Terrestrial planet evolution strongly depends on the regime of mantle convection. Assuming that brittle failure limits the strength of the lithosphere, our simulations indicate that the effects of lithosphere hydration dominate the effects of planetary mass on yield and convective stresses. Modeling results for super-Venus planets, however, suggest two additional mechanisms for escaping the stagnant-lid regime. First, massive terrestrial planets in the stagnant-lid regime feature crustal temperature profiles that enter the stability field of eclogite after crust grows beyond a critical thickness. If a sufficiently large fraction of the total crustal thickness is composed of eclogite, the entire crust could be gravitationally unstable and susceptible to floundering because eclogite is intrinsically denser than mantle peridotite.

On Earth, the phase transition from (metamorphosed) basalt to eclogite primarily occurs in subduction zones. Eclogite is also formed during continent-continent collisions such as the Eurasian and Indian plate collisions (Bucher and Frey, 2002). Furthermore, the high density of eclogite is theorized to have caused delimitation, foundering, and recycling of relatively thick oceanic lithosphere on Earth during the Archaean (Vlaar et al., 1994). Because massive terrestrial planets have relatively high surface gravity, the phase transition to eclogite will occur at a relatively shallow depth, making eclogite the stable mineral phase for a large fraction of the crust. The formation of a thick eclogite layer then could cause lithosphere floundering or intermittent plate tectonics, a more extreme version of episodic subduction mechanisms proposed for Venus (Turcotte, 1993; Fowler and O'Brien, 1996).

In thermal evolution models, the heat conduction equation is numerically solved to calculate crustal temperatures. An approximate temperature profile can also be calculated using a steady-state approximation as (Turcotte and Schubert, 2002)

$$T(z) = T_s + \frac{F_s}{k} z - \frac{Q_c(t_p)}{2k} z^2, \tag{38}$$

where Q_c, the volumetric crustal heat production, is calculated as

$$Q_c(t_p) = Q_0 e^{-\lambda t_p} \left(\frac{V_{proc}(t_p)}{V_c(t_p)} \right), \tag{39}$$

where t_p is 4.5 Gyr and V_c is the volume of the crust. The boundary condition $T(h_c) = T_c$ is used to calculate surface heat flux for specified Moho and surface temperatures and magnitude of internal heat production. Finally, Eq. 38 is used to calculate the temperature

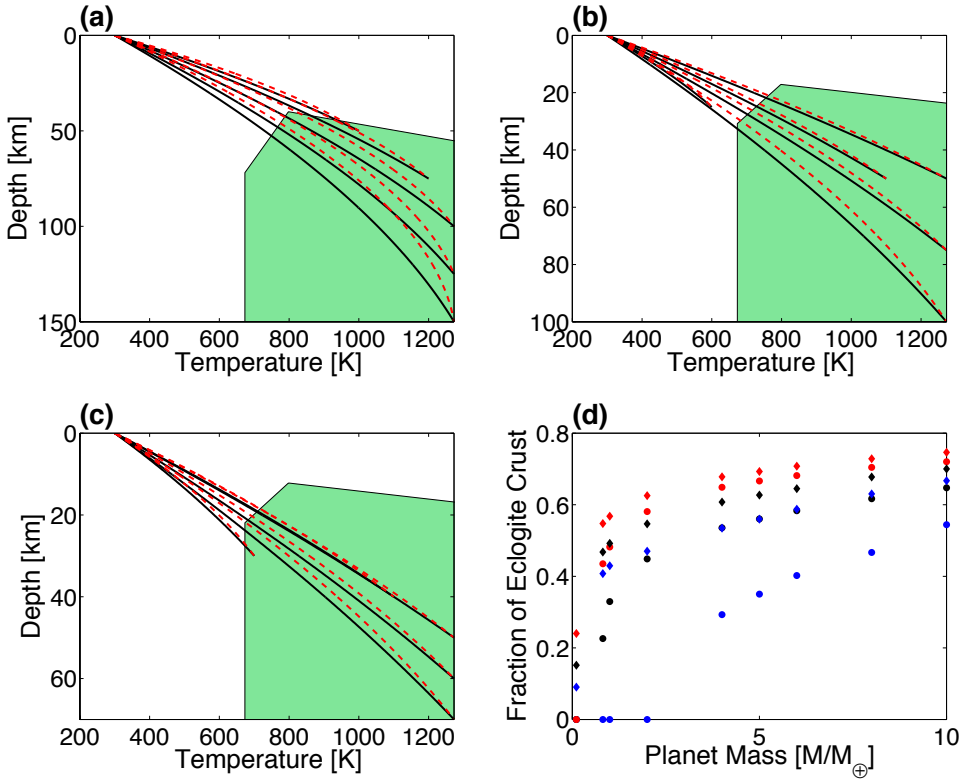

Figure 12: Crustal temperature profiles for (a) Venus and (b) $5M_{\oplus}$ and (c) $10M_{\oplus}$ super-Venus planets, calculated assuming representative crustal thicknesses, degrees of mantle processing, and Moho temperatures. The green shaded area is the approximate stability field for eclogite, drawn using the phase diagram from Philpotts and Ague (2009). Black solid and red dashed lines represent Venus-equivalent $Q_0 = 1.0 \times 10^{-7}$ and 1.75×10^{-7} W m^{-3}, respectively. Panel (d) shows the fraction of crust in the eclogite phase for Mars, Venus, and seven super-Venus planets. Circles and triangles represent $T_u(0) = 1700$ and 2000 K, respectively. Blue, black, and red symbols represent Venus-equivalent $Q_0 = 5.0 \times 10^{-8}$, 1.0×10^{-7}, and 1.75×10^{-7} W m^{-3}, respectively.

profile throughout the entire thickness of the crust. Representative temperature profiles for a planet can be used to determine the fraction of crust that lies within the eclogite stability field.

Figure 12 shows representative temperature profiles for Venus and 5 and $10M_{\oplus}$ super-Venus planets, calculated using representative crustal thicknesses, degrees of mantle processing, and Moho temperatures from the previous sensitivity analyses. A range of internal radiogenic heating was also considered. Panel (d) in Fig. 12 summarizes the effects of initial conditions on the fraction of crust in the eclogite stability region after 4.5 Gyr. For Mars, Venus, and seven super-Venus planets, 54 thermal evolution simulations were run to study

all permutations of the initial conditions $T_u(0) = 1700$ and 2000 K and Venus-equivalent $Q_0 = 0.5$, 1.0, and 1.75 $\times 10^{-7}$ W m^{-3}. In general, the fraction of eclogite crust increases with planetary mass.

Representative temperature profiles for massive terrestrial planets pass through the eclogite stability field for plausible initial conditions. For super-Venus planets with masses greater than $\sim 4 M_\oplus$, eclogite may be the stable phase for the majority of the crust unless the initial mantle potential temperature or magnitude of internal heating is very low. So, crust material may undergo a phase transition to eclogite at relatively shallow depths as the crust grows during thermal evolution in the stagnant-lid regime, forming a thick eclogite layer that could subsequently flounder. As long as crustal production continues, eclogite formation and floundering could occur periodically, possibly yielding a regime of mantle convection resembling intermittent plate tectonics. Although this study suggests that this process is plausible, pursuing its dynamics in detail is left for future studies.

Second, high surface and crustal temperatures may also cause periodic transitions from the stagnant-lid regime to a form of mobile-lid convection. In this work, massive terrestrial planets in the stagnant-lid regime with surface temperatures held constant at 300 K tend to have very hot crusts. If high surface temperatures exist alongside high crustal temperatures, a transition from stagnant-lid convection to a mobile-lid regime can occur (Reese et al., 1999). Feedback between a changing mantle convection regime and a periodic atmospheric greenhouse effect driven by varying amounts of volcanism, for instance, may be very important to the evolution of Venus (Noack et al., 2012). As surface temperature depends on atmospheric mass and composition and the luminosity of the central star, however, this possibility of escaping the stagnant-lid regime may not be as robust as the first mechanism based on the formation of self-destabilizing crust

6 Conclusions

Terrestrial planet evolution is complicated. Although plate tectonics is observed on Earth, the stagnant-lid regime of mantle convection may be most natural for terrestrial planets; at least, it is most common in our Solar System. Thermal evolution models in this study yield first-order conclusions about the evolution of Mars, Venus, and super-Venus planets. For Mars and Venus, principal component analysis of simulation results conducted with a wide range of initial conditions captures the relationships between the large number of parameters that describe the interior of a planet. Depending on initial conditions, Mars and

Venus could have evolved along a variety of paths, featuring different crustal thicknesses and temperatures, interior temperatures, and degrees of mantle processing. To produce specific histories consistent with spacecraft data obtained from Mars and Venus, complications must be added to these simple models.

Properties of massive terrestrial exoplanets are poorly constrained, so questions about the effects of planetary mass on the likelihood of plate tectonics and other important planetary parameters await answers. Simple scaling analyses indicate that mantle melt productivity should increase with planetary mass. Because the increase in mantle processing is slow, however, crustal thickness and the relative fraction of processed mantle actually decrease with increasing planetary mass, as thermal evolution simulations confirm. Surface gravity increases with planetary mass, so pressure in the crust of massive terrestrial planets increases relatively rapidly with depth. Plausible temperature profiles favor a phase transition to gravitationally unstable eclogite during normal crustal formation, whereas the basalt to eclogite transformation rarely occurs aside from subduction on Earth. Therefore, thick eclogite layers, along with mobile, hot crust material, may be important to the evolution of massive terrestrial planets.

Part II

Thermal evolution of Venus with argon degassing

1 Introduction

Observations of Venus can constrain its evolution throughout geologic time. Most notably, Venus currently lacks plate tectonics (e.g., Kaula and Phillips, 1981). Instead, convection proceeds in the stagnant-lid regime (e.g., Solomatov and Moresi, 1996; Nimmo and McKenzie, 1998; Schubert et al., 2001). Because Venus lacks surface water, its crust is highly vicious and its upper mantle is stiff (Kaula, 1995; Mackwell et al., 1998). Greenhouse gases CO_2 and H_2O have raised surface temperatures to roughly 740 K (e.g., Bullock and Grinspoon, 2001). Furthermore, the age of latest resurfacing for the vast majority of the surface of Venus is roughly 300 Myr to 1 Gyr (McKinnon et al., 1997; Nimmo and McKenzie, 1998; Hauck et al., 1998), and the distribution of craters on the volcanic plains on Venus cannot be distinguished from a random distribution (Strom et al., 1994). No global resurfacing event has occurred in the last $\sim$500 Myr, but evidence from current SO_2 levels in the atmosphere of Venus (Bullock and Grinspoon, 2001) and from spacecraft observations of hotspot emissivity (Smrekar et al., 2010) indicate that Venus is geologically active at the present.

Several evolutionary scenarios have been posited to explain these observations. First, many studies invoke a catastrophic resurfacing event with varying magnitudes of previous and subsequent volcanic activity to account for the crater distribution on Venus (e.g., Schaber et al., 1992; Strom et al., 1994; Romeo and Turcotte, 2010). Mechanisms for a resurfacing event include episodic subduction caused by lithosphere thickening above a warming mantle (Turcotte, 1993; Fowler and O'Brien, 1996) and brittle mobilization of the lithosphere (Moresi and Solomatov, 1998). Second, some models attempt to couple the evolution of both the interior and atmosphere of Venus (e.g., Phillips et al., 2001; Noack et al., 2012). High temperatures may provoke a transition into an episodic or stagnant-lid regime by strengthening the lithosphere through a higher healing rate in damage rheology (Landuyt and Bercovici, 2009) or by increasing the mantle temperature and thus causing convective stress to drop below the lithosphere yield stress (Lenardic et al., 2008). Mantle

convection models that include greenhouse warming of the atmosphere may feature periodic increases in surface temperature to ∼1000 K (Noack et al., 2012), which indicate possible transitions from the stagnant-lid to mobile-lid regime of mantle convection (Reese et al., 1999). Finally, some suggest that the young-looking surface of Venus represents a transition from the plate tectonic to stagnant-lid regime that occurred between 1 Gyr and 500 Myr ago (e.g., Phillips and Hansen, 1998). Unfortunately, observations of the Venusian surface provide few constraints on thermal evolution of Venus before 1 Gyr ago.

The present-day atmospheric mass of radiogenic ^{40}Ar provides insight into the history of Venus that is not preserved in the surface geologic record. Earth's budget of radiogenic argon has long been used to place constraints on its evolution (e.g., Allègre et al., 1996). For Venus, the degassing of radiogenic argon has only been used to test the plausibility of various scenarios for crustal production featuring arbitrary numbers of discrete resurfacing events (Namiki and Solomon, 1998; Kaula, 1999). No previous work has used argon degassing in simulations of the thermal and chemical evolution of the interior of Venus that include crustal production.

The purpose of this study is to use the parametrized model of stagnant-lid convection detailed in Part I of this thesis to generate an evolutionary model for Venus consistent with observational constraints. Two end-member evolutionary scenarios are considered. First, the effects of a single catastrophic resurfacing event on the atmospheric mass of radiogenic argon are studied, following Kaula (1999). Next, argon degassing is incorporated into our parametrized convection model, which is modified from Part I to include the effects of mantle plumes and to more accurately calculate radiogenic internal heating. Simulations are conducted for a range of abundances of heat-producing elements, mantle potential temperatures, and core/mantle boundary temperatures. Then, best-fit linear functions are derived to approximate model output from initial conditions. Using these functions, the space of initial conditions that will yield present-day parameter values consistent with observational constraints can be predicted.

2 Theoretical formulation

The present-day atmospheric mass of radiogenic argon can be used to constrain the thermal and chemical evolution of Venus. In this section, we begin to explore the plausibility of different scenarios. First, we consider a single resurfacing event. Next, we incorporate argon degassing into our thermal evolution model. Finally, we present a simple model

for upwelling plumes to determine if they may significantly influence the history of argon degassing and explain the surface geology of Venus.

2.1 Closed-system evolution of the mantle

As a simple problem, we consider closed-system of the mantle until a single resurfacing event at $t_r = 4.0$ Gyr that produces crustal thickness h_c. Until the resurfacing event, ^{40}Ar accumulates in the mantle from the decay of ^{40}K with no degassing. We assume the following effective abundances and ratios for the primitive mantle at the present (Kaula, 1999): [U] = 21 ppb, K/U = 7220 ± 1220, and $[^{40}\mathrm{K}]/[\mathrm{K}] = 1.165\times10^{-4}$. We thus calculate an effective present-day abundance of ^{40}K in the primitive mantle of $[^{40}\mathrm{K}(t_p)]_{PM} = 17.66$ ppb. A lower bound for Earth's mantle is [U] = 13 ppb (Lyubetskaya and Korenaga, 2007), for which $[^{40}\mathrm{K}(t_p)]_{PM} = 10.93$ ppb. Using these values, we can quantify the effects of a single resurfacing event on the planetary budget of K, ^{40}K, and ^{40}Ar.

The primordial abundance of ^{40}K is

$$[^{40}\mathrm{K}(0)]_{PM} = [^{40}\mathrm{K}(t_p)]_{PM} \exp[(\lambda_{Ar} + \lambda_{Ca})t_p), \tag{40}$$

where λ_{Ar} and λ_{Ca} are the decay constants for the decay of ^{40}K to ^{40}Ar and ^{40}Ca, respectively, from Table 8. The abundances of ^{40}K and ^{40}Ar in the primitive mantle at a time $t \leq t_r$ can be calculated:

$$[^{40}\mathrm{K}(t)]_{PM} = [^{40}\mathrm{K}(0)]_{PM} \exp[-(\lambda_{Ar} + \lambda_{Ca})t] \tag{41}$$

and

$$[^{40}\mathrm{Ar}(t)]_{PM} = \frac{\lambda_{Ar}}{\lambda_{Ar} + \lambda_{Ca}}[^{40}\mathrm{K}(0)]_{PM} \left(1 - \exp[-(\lambda_{Ar} + \lambda_{Ca})t]\right), \tag{42}$$

because ^{40}K and ^{40}Ar have the same mass. Likewise, we have:

$$[\mathrm{K}(t)]_{PM} = [\mathrm{K}(0)]_{PM} - [^{40}\mathrm{K}(0)]_{PM} \left(1 - \exp[-(\lambda_{Ar} + \lambda_{Ca})t]\right). \tag{43}$$

For a given crustal thickness h_c, the necessary crustal volume V_c can be calculated with a geometrical relation (Fraeman and Korenaga, 2010):

$$V_c = \frac{4\pi}{3}\left[R_p^3 - (R_p - h_c])^3\right], \tag{44}$$

Table 8: Summary of constants used for radiogenic heat production taken from Kaula (1999) and Korenaga (2006).

Isotope	λ_n [1/Gyr]	P_n [μW/kg]
^{238}U	0.155	93.7
^{235}U	0.985	569
^{232}Th	0.0495	26.9
^{40}K to ^{40}Ar	0.0581	1.02
^{40}K to ^{40}Ca	0.4962	26.69

where R_p is the radius of the planet. Assuming that crust is formed by partial melting of the mantle with melt fraction ϕ, the volume of mantle that must be processed to produce the crust with thickness h_c is $\Delta V_{proc} = V_c/\phi$.

Argon-40 partitioning is assumed to follow the following formula for accumulated fractional melting (Shaw, 1970):

$$\frac{[^{40}\mathrm{Ar}(t_r)]_c}{[^{40}\mathrm{Ar}(t_r)]_{PM}} = \frac{1}{\phi}\left[1-(1-\phi)^{1/D}\right], \tag{45}$$

where $[^{40}\mathrm{Ar}(t_r)]_c$ is the concentration of ^{40}Ar in the melt that forms the crust and D is the bulk distribution coefficient. Because D is very small (e.g., Kaula, 1999), we approximate $[^{40}\mathrm{Ar}(t_r)]_c/[^{40}\mathrm{Ar}(t_r)]_{PM} \approx 1/\phi$ for simplicity. We likewise approximate $[\mathrm{K}(t_r)]_c/[\mathrm{K}(t_r)]_{PM} \approx 1/\phi$. Assuming that all ^{40}Ar from the processed mantle is released to the atmosphere, the mass of ^{40}Ar released to the atmosphere during the resurfacing event can be calculated:

$$M_{Ar,r} = [^{40}\mathrm{Ar}(t_r)]_{PM}\frac{\rho_m V_c}{\phi}, \tag{46}$$

where ρ_m is the density of the mantle. Additional ^{40}Ar may be released into the atmosphere from the decay of ^{40}K sequestered in the crust, if the crust is sufficiently hot so that intragranular argon diffusivity is high (Kaula, 1999). One experimental study argues that ^{40}Ar is more compatible with olivine than with basalt melt and has very low diffusivity in the major phases of terrestrial planets (Watson et al., 2007), but recent work supports our assumptions (Cassata et al., 2011). The mass of ^{40}Ar released from the crust in the time between t_r and t_p is therefore:

$$M_{Ar,d} = \rho_m V_c [^{40}\mathrm{K}(t_r)]_c \frac{\lambda_{Ar}}{\lambda_{Ar}+\lambda_{Ca}}\left(1-\exp[-(\lambda_{Ar}+\lambda_{Ca})(t_p-t_r)]\right). \tag{47}$$

The total mass of atmospheric ^{40}Ar at the present is thus $M_{Ar} = M_{Ar,r} + M_{Ar,d}$. Finally, the crustal abundances of ^{40}K and K after the resurfacing event are

$$[^{40}\mathrm{K}(t_r)]_c = \frac{[^{40}\mathrm{K}(t_r)]_{PM}}{\phi} \tag{48}$$

and

$$[\mathrm{K}(t_r)]_c = \frac{[\mathrm{K}(t_r)]_{PM}}{\phi}. \tag{49}$$

Predictions from this simple model may be compared to data from landers or incorporated into more complex scenarios for the thermal history of Venus.

2.2 Mass transport of argon during stagnant-lid convection

To simulate the thermal and chemical evolution of Venus, we used the model described in Part I with some modifications. In particular, we incorporate the formulation used to track the mass transport of water and heat producing elements in Fraeman and Korenaga (2010) to parametrize argon degassing. To that end, we consider heat production from the radioactive decay of ^{40}K, ^{235}U, ^{238}U, and ^{232}Th instead of modeling radiogenic heat production with a single effective decay constant as in Stevenson et al. (1983). Volumetric radiogenic heating may be calculated (Korenaga, 2006):

$$H(t) = \rho_m \sum_n c_{n,0} P_n(0) \exp(-\lambda_n t), \tag{50}$$

where, for each isotope, $c_{n,0}$ is the initial abundance, $P_n(0)$ is the initial specific heat production, and λ_n is the decay constant. Table 8 summarizes the relevant constants involved in calculating radiogenic heat production. Initial isotopic abundances are calculated from the present-day abundance of uranium, assuming that the following ratios are valid at the present for the primitive mantle (Kaula, 1999; Korenaga, 2006): K/U = 7220, ^{40}K/K = 1.165×10^{-4}, ^{238}U/U = 0.9927, ^{235}U/U = 0.0072, and ^{232}Th/U = 4.

We track the degassing of ^{40}Ar with the method that Fraeman and Korenaga (2010) used to track the dehydration of the mantle. The amount of mantle that has been melted during a time interval Δt is (Fraeman and Korenaga, 2010):

$$\Delta V_{proc}(t) = \frac{f_m(t)}{\phi} \Delta t, \tag{51}$$

where $f_m(t)$ is the whole-planet melt productivity and ϕ is the melt fraction. We track the abundance of ^{40}K in the primitive mantle:

$$[^{40}\mathrm{K}(t)]_{PM} = [^{40}\mathrm{K}(0)]_{PM} \exp[-(\lambda_{Ar} + \lambda_{Ca})t], \tag{52}$$

where $[^{40}\mathrm{K}(0)]_{PM}$ is the initial abundance of ^{40}K in the primitive mantle. Next, we track the mass and abundance of ^{40}K in the crust using two equations:

$$M_{c,^{40}K}(t) = M_{c,^{40}K}(t - \Delta t) \exp[-(\lambda_{Ar} + \lambda_{Ca})\Delta t] + \rho_c [^{40}\mathrm{K}(t)]_{SM} \Delta V_{proc} \tag{53}$$

and

$$[^{40}\mathrm{K}(t)]_c = \frac{M_{c,^{40}K}(t)}{\rho_c V_c}, \tag{54}$$

where $\rho_c \approx \rho_m$ is the density of the crust and V_c is the volume of the crust.

The abundance of ^{40}Ar in the primitive mantle is:

$$[^{40}\mathrm{Ar}(t)]_{PM} = \frac{\lambda_{Ar}}{\lambda_{Ar} + \lambda_{Ca}} [^{40}\mathrm{K}(0)]_{PM} \left(1 - \exp[-(\lambda_{Ar} + \lambda_{Ca})t]\right), \tag{55}$$

and the mass of ^{40}Ar in the primitive mantle is:

$$M_{PM,^{40}Ar}(t) = \rho_m V_{PM} [^{40}\mathrm{Ar}(t)]_{PM}. \tag{56}$$

The mass of ^{40}Ar released into the crust during partial melting of the mantle may be calculated:

$$M_{c,^{40}Ar}(t) = M_{c,^{40}Ar}(t - \Delta t) + \rho_c \Delta V_{proc} [^{40}\mathrm{Ar}((t - \Delta t))]_{SM}, \tag{57}$$

where the abundance of ^{40}Ar in the source mantle is tracked:

$$[^{40}\mathrm{Ar}(t)]_{SM} = \frac{M_{PM,^{40}Ar}(t) - M_{c,^{40}Ar}(t)}{\rho_c V_{SM}(t)}, \tag{58}$$

where $V_{SM}(t)$ is the volume of the source mantle.

The decay of crustal ^{40}K also increases the crustal abundance of ^{40}Ar. The mass of ^{40}Ar produced in the crust during Δt is,

$$\Delta M_{c,^{40}Ar}(t) = \rho_c V_c \frac{\lambda_{Ar}}{\lambda_{Ar} + \lambda_{Ca}} [^{40}\mathrm{K}(t)]_c \left(1 - \exp[-(\lambda_{Ar} + \lambda_{Ca})\Delta t]\right). \tag{59}$$

Finally, assuming that crustal temperatures are sufficiently high to allow argon to diffuse

out of mineral grains within Δt (Kaula, 1999; Cassata et al., 2011), the total mass of ^{40}Ar released to the atmosphere of Venus may be tracked at each time step:

$$M_{atm,^{40}Ar}(t) = M_{atm,^{40}Ar}(t - \Delta t) + M_{c,^{40}Ar}(t) - M_{c,^{40}Ar}(t - \Delta t) + \Delta M_{c,^{40}Ar}(t). \quad (60)$$

2.3 Upwelling mantle plumes

Upwelling plumes from the core/mantle boundary may transport heat to the top of the mantle if there exists a thermal boundary layer at the bottom of the mantle with temperature difference $\Delta T > 0$. The maximum volume of material available to form plumes is $V_p = 4\pi R_c^2 \delta_c$, where δ_c is the thickness of the thermal boundary layer on the mantle side of the core/mantle boundary and R_c is the radius of the core. Material in the thermal boundary layer is replenished on time scale $\tau = \delta_c^2/\kappa$, where κ is thermal diffusivity. The maximum volumetric flux of plume material that can be delivered to the lithosphere in time Δt is therefore (Weizman et al., 2001):

$$S_{p,max} = \Delta t \left(\frac{V_p}{\tau} \right) = \Delta t \left(\frac{4\pi R_c^2 \kappa}{\delta_c} \right). \quad (61)$$

Only a fraction of the boundary layer will actually form plumes. The rate of heat delivery by plumes may be expressed as an additional contribution to the mantle heat flux (Weizman et al., 2001):

$$F_p = S_p \left(\frac{\rho_m C_m \Delta T}{4\pi (R_p - h_c)^2} \right), \quad (62)$$

where ΔT is the plume temperature anomaly. We assume that the heat flux from plume upwelling is some fraction of the core heat flux, i.e. $F_p = f(R_c/R_p)^2 F_c$, where $0 \leq f < 1$ and R_p is the radius of Venus. Thus, we may calculate:

$$S_p = f F_c \left(\frac{R_c}{R_p} \right)^2 \left(\frac{4\pi (R_p - h_c)^2}{\rho_m C_m \Delta T} \right), \quad (63)$$

where $S_p \ll S_{p,max}$ is guaranteed. The effective mantle heat flux then becomes $F'_m = F_m + F_p$, where F_m is the mantle heat flux from sublithospheric convection.

We assume that the upwelling plume reaches the base of the lithosphere within the time step of duration Δt and undergoes partial melting. The initial pressure of plume melting,

$P_{i,p}$, is related to the potential temperature of the mantle plumes as

$$P_{i,p} = \frac{T_{u,p} - 1423}{120 \times 10^{-9} - (dT/dP)_S}, \tag{64}$$

where $T_{u,p} = T_u + \Delta T$ is the potential temperature of the mantle plumes, i.e. the temperature that it would have if it were raised from the core/mantle boundary to the surface along an adiabatic temperature gradient. The final pressure of melting and the average melt fraction in the melting region are calculated using equations 10 and 11. Finally, the melt productivity of the mantle plumes is simply $f_p = \phi S_p$, assuming that the entire plume passes through the region of melting.

3 Numerical models

The histories calculated using the simple parametrized evolution model in Part I were not intended to precisely reconstruct the thermal and chemical evolution of Venus. But with the addition of further complications, more plausible scenarios may be formulated. Therefore, we perform additional simulations using the modifications necessary to track the degassing of radiogenic argon. In particular, the following sets of initial conditions were used: present-day uranium abundance, $[^{40}\mathrm{U}(t_p)]_{PM}$ = 13, 15, 17, 19, and 21 ppb; initial mantle potential temperature, $T_u(0)$ = 1300, 1400, 1500, 1600, and 1700 K; initial core/mantle boundary temperature, $T_{cm}(0)$ = 3500, 3750, 4000, 4250, and 4500 K; reference viscosity, $\eta_0 = 10^{18}$, 10^{19}, and 10^{20} Pa s; dehydration stiffening, $\Delta\eta_w = 100$; and compositional buoyancy, $d\rho/d\phi$ = 120 kg m^{-3}.

Tighter constraints were placed on these simulations than in Part I. In particular, no inner core growth can occur; 2 km $\leq h_c(t_p) \leq$ 100 km; and $F_s(t_p) > 0$ mW m^{-2}. Thirty-four of 314 simulations failed these criteria, primarily those that featured either extremely high or low values of both $[^{40}\mathrm{U}(t_p)]_{PM}$ and $T_u(0)$. Present-day $[^{40}\mathrm{U}]_{PM}$ = 21 and 13 ppb are equivalent to the initial volumetric magnitudes of radiogenic heating $Q_0 = 7.07 \times 10^{-8}$ and 4.38×10^{-8} mW m^{-3}, respectively. An additional model output parameter for these simulations is t_{plume}, the time at which core cooling, and thus mantle plume upwelling, resumes after the loss of the transient "hot-start".

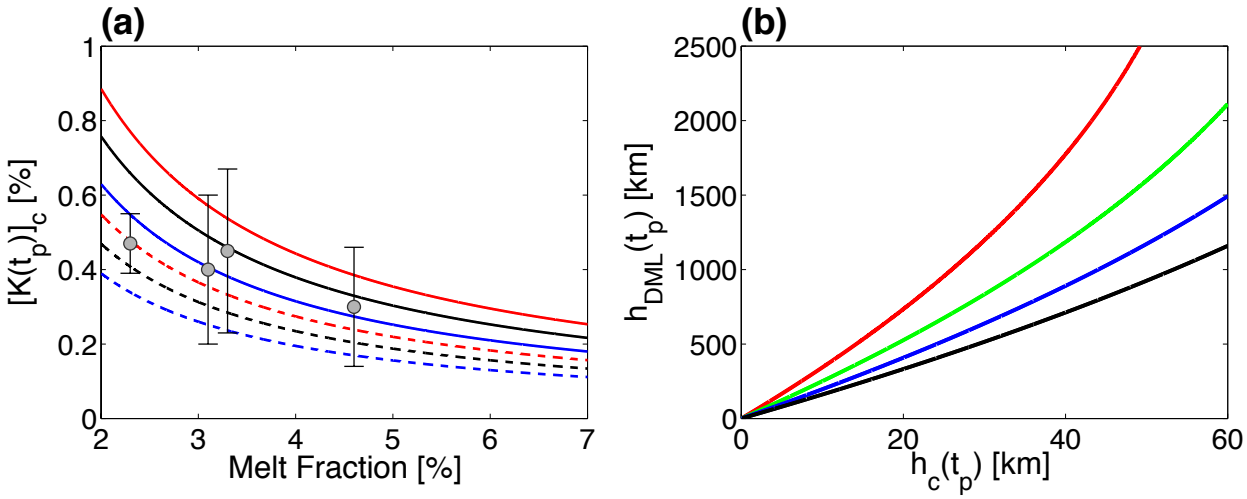

Figure 13: Panel (a): present-day ($t_p = 4.5$ Gyr) abundance of potassium as a function of average melt fraction during the resurfacing event at $t_r = 4.0$ Gyr. Blue, black, and red lines represent present-day K/U = 6000, 7220 and 8440, respectively. Solid and dashed lines represent $[\mathrm{U}(t_p)]_{PM} = 21$ and 13 ppb, respectively. Grey dots with error bars are measurements from the Venera 9, Venera 10, Vega 1, and Vega 2 landers, with partial melt percentages calculated in Kaula (1999). Panel (b): Thickness of the resulting depleted mantle lithosphere layer as a function of the crustal thickness produced during the resurfacing event. Black, blue, green, and red lines signify, respectively, $\phi = 0.06$, 0.05, 0.04, and 0.03.

4 Results

Different scenarios for the thermal and chemical evolution of Venus yield different predictions for present-day crustal thickness and the atmospheric mass of radiogenic argon. In this section, we investigate two end-member scenarios: a single episode of crustal production and continuous evolution in the stagnant-lid regime.

4.1 A single catastrophic resurfacing event

Figure 13 shows the present-day crustal abundance of potassium predicted for closed-system evolution of the mantle with a single resurfacing event for present-day K/U = 7220 ± 1220 and $[\mathrm{U}(t_p)]_{PM} = 21$ and 13 ppb. Measurements of potassium abundance by four Soviet landers, as a function of calculated melt fraction, are also plotted. All of the tested K/U and $[\mathrm{U}(t_p)]_{PM}$ are consistent with the measured crustal $[\mathrm{K}(t_p)]$ in this model. The thicknesses of the mantle layer that would be processed to produce a range of crustal thickness are also shown in Fig. 13 for $\phi = 0.06$, 0.05, 0.04, and 0.03.

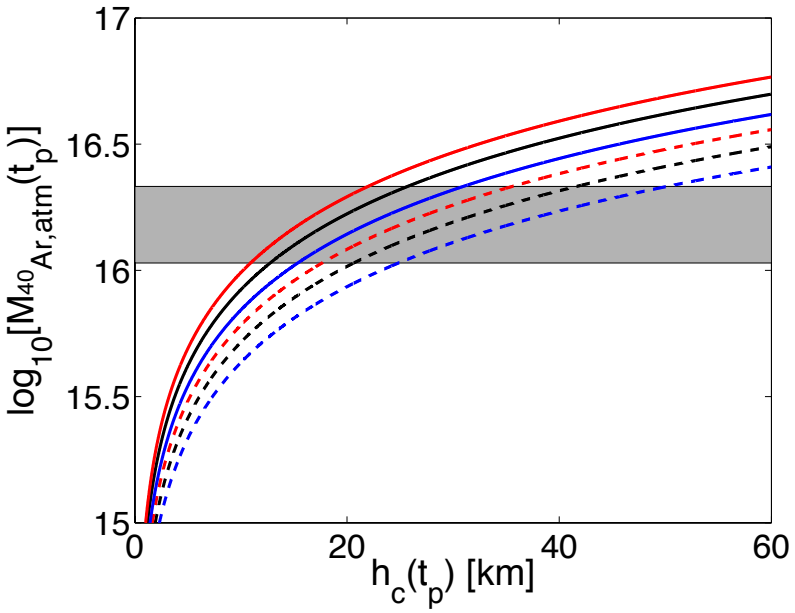

Figure 14: Predictions of the present-day atmospheric mass of radiogenic ^{40}Ar released as a consequence of a resurfacing event at $t_r = 4.0$ Gyr as a function of crustal thickness. We assume $\phi = 0.04$. Solid and dashed lines represent $[\mathrm{U}(t_p)]_{PM} = 21$ and 13 ppb, respectively. Blue, black, and red curves respectively represent K/U = 6000, 7220, and 8440. The possible range of present-day atmospheric mass of ^{40}Ar from Kaula (1999) is shaded in grey.

Figure 14 shows the output of calculations of the mass of atmospheric ^{40}Ar with $\phi = 0.04$ as a function of crustal thickness for different present-day uranium abundances and K/U ratios. The present-day mass of ^{40}Ar in the atmosphere of Venus is $1.61 \pm 0.54 \times 10^{16}$ kg (Kaula, 1999), and this range is indicated in Fig. 14. With $[\mathrm{U}(t_p)]_{PM} = 21$ ppb and present-day K/U = 7220, a resurfacing event that produced a final crustal thickness of approximately 20 ± 10 km would release an amount of ^{40}Ar consistent with the present-day atmospheric composition of Venus. Decreasing the present-day uranium abundance to 13 ppb increases the plausible values of crustal thickness to roughly 33 ± 18 km.

4.2 Argon degassing during stagnant-lid convection

The output of 314 simulations of the thermal evolution of Venus are shown in Fig. 15. Thirty-four simulations were excluded because they did not meet the requirements that 2 km $\leq h_c \leq$ 100 km and inner core growth not occur. Interesting present-day parameters are plotted against present-day crustal thickness. The first principal component eigenvector is projected onto each plot, emanating from the average simulation output, to show the

first-order correlations between output parameters. The largest coefficients in the principal component eigenvector are associated with T_c (0.33), h_c (0.31), and ΔV_{proc} (0.30). That is, a thicker crust is correlated with a hotter crust and a higher degree of mantle processing, and vice versa. The coefficients for some other model output parameters are negative, such as T_u (-0.18), h_l (-0.28), h_{TBL} (-0.26), and t_{plume} (-0.29). So, as seen in Fig. 15, a thicker crust is associated with a colder mantle, thinner mantle lithosphere, and an earlier resumption of core cooling. This single principal component accounts for the majority ($\sim$55%) of the variance in the model output data set.

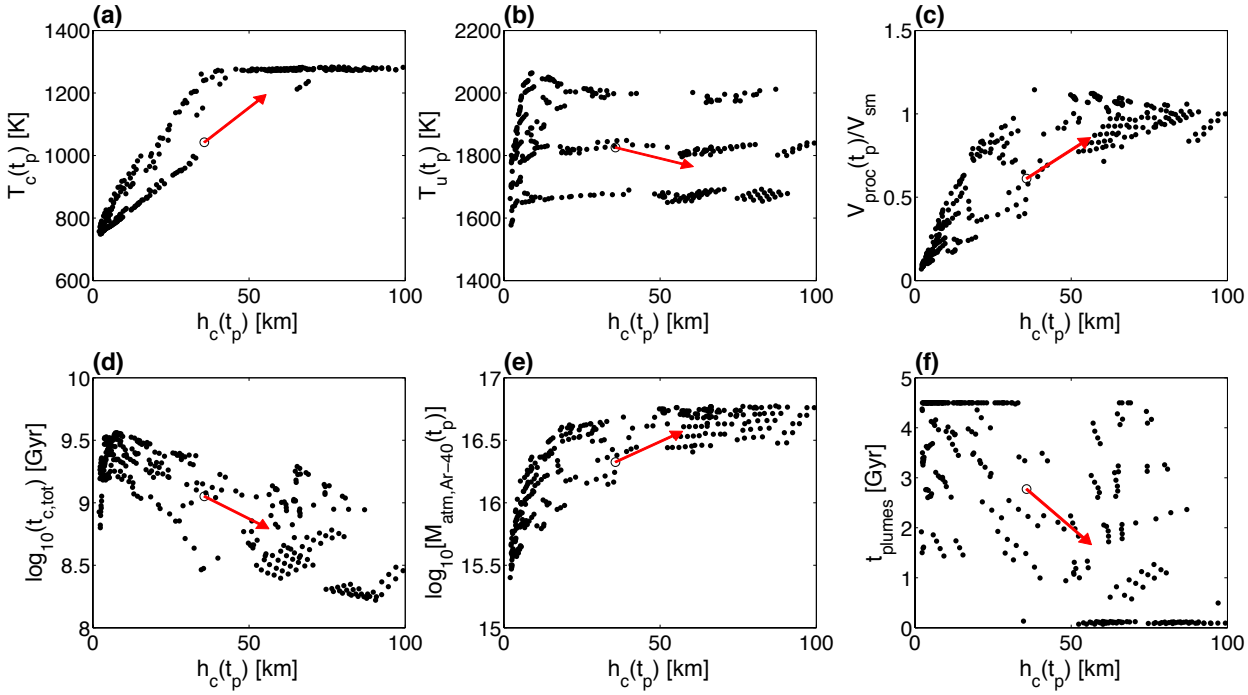

Figure 15: Summary of parameter values at the present for 314 simulations of the thermal evolution of Venus. The red arrow is a projection of the first principal component basis vector, emanating from a point representing the averaged simulation results, that indicates the axis accounting for the majority of the variance in the data set. Panels show (a) Moho temperature, (b) mantle potential temperature, (c) fraction of mantle processed by melting, (d) total time for crust to grow from 10% to 95% of its present thickness, (e) present-day atmospheric mass of radiogenic argon, and (f) the time at which core cooling, and thus plume upwelling, began to occur as functions of crustal thickness.

Present-day model parameters can be roughly predicted with a linear function of initial conditions, using Eq. 25 with the assumption that $A_{i,4} = 0$. Table 9 lists coefficients for the best-fit approximation to output parameters after 4.5 Gyr that have a correlation

coefficient > 0.80 between predicted values and model output. Interesting parameters like h_c and $\log_{10}[M_{atm,Ar}(t_p)]$ have correlation coefficients > 0.90. To use the best-fit function with the listed coefficients, the input and output data sets must first be mean subtracted and normalized using the listed average and standard deviations for each parameter.

Figure 16 illuminates the predictive power of the best-fit linear functions for six interesting model parameters. For example, while crustal thickness is well-predicted in general, the best-fit function underestimates crustal thickness for $h_c < 10$ km. Likewise, the best-fit function for Moho temperature returns poor predictions for the coldest and hottest temperatures. Basal melting in the crust causes non-linearity for high Moho temperatures, whereas the large number of simulations with extremely cold initial conditions harms the fit for Moho temperatures close to T_s. Parameters such as T_u, ΔV_{proc}, and $\log_{10}[M_{atm,Ar}(t_p)]$, however, are relatively well approximated. Finally, although predictions of $t_p > 4.5$ Gyr may be accurate, stopping the simulation at $t_p = 4.5$ Gyr introduces non-linearity because an insufficient length of time is provided for core cooling to occur.

B_i	$A_{i,0}$	$A_{i,1}$	$A_{i,2}$	$A_{i,3}$	$A_{i,5}$	Units	Corr.
T_c	1042	129	139	-129	72.8	K	0.90
T_u	1826	14.7	16.7	113	29.3	K	0.95
T_{cm}	3159	71.2	78.8	118	16.2	K	0.94
h_c	35.7	18.7	20.4	-14.7	12.0	km	0.92
h_l	101	-8.42	-9.13	36.4	1.34	km	0.94
h_{ML}	109	-6.00	-6.54	31.1	1.93	km	0.93
C^w_{sm}	0.60	-0.12	-0.13	0.12	-0.13	-	0.91
V_{proc}/V_{sm}	0.61	0.19	0.20	-0.18	0.22	-	0.91
$\log_{10}(\Delta t_{c,tot})$	9.05	-0.15	-0.17	0.28	-0.01	-	0.81
$\log_{10}[M_{atm,Ar}(t_p)]$	16.33	0.19	0.21	-0.18	0.27	-	0.93
t_{plume}	2.77	-0.65	-0.72	1.40	0.09	Gyr	0.90

Table 9: Coefficients for the best-fit linear function (Eq. 25 with $A_{i,4} = 0$) relating parameter values after 4.5 Gyr for parameters with correlation coefficients > 0.80 to a given set of initial conditions for Venus. Correlation coefficients quantifying the correspondence between the actual and predicted output parameters were calculated using normalized and mean subtracted input and output parameters. The average values of the input parameters are $T_u(0) = 1497$ K, $T_{cm}(0) = 3994$ K, $\log_{10}(\eta_0) = 19.09$, and $[\mathrm{U}(t_p)]_{PM} = 17.23$ ppb. For the best-fit function, the input parameters are mean subtracted and normalized by 137 K, 341 K, 0.80, and 2.79 ppb, respectively.

Linear functions for key model results can be used to quickly predict whether a given set of initial conditions will yield present-day parameters consistent with observational constraints without repeating numerical simulations. Figure 17 shows ranges of initial

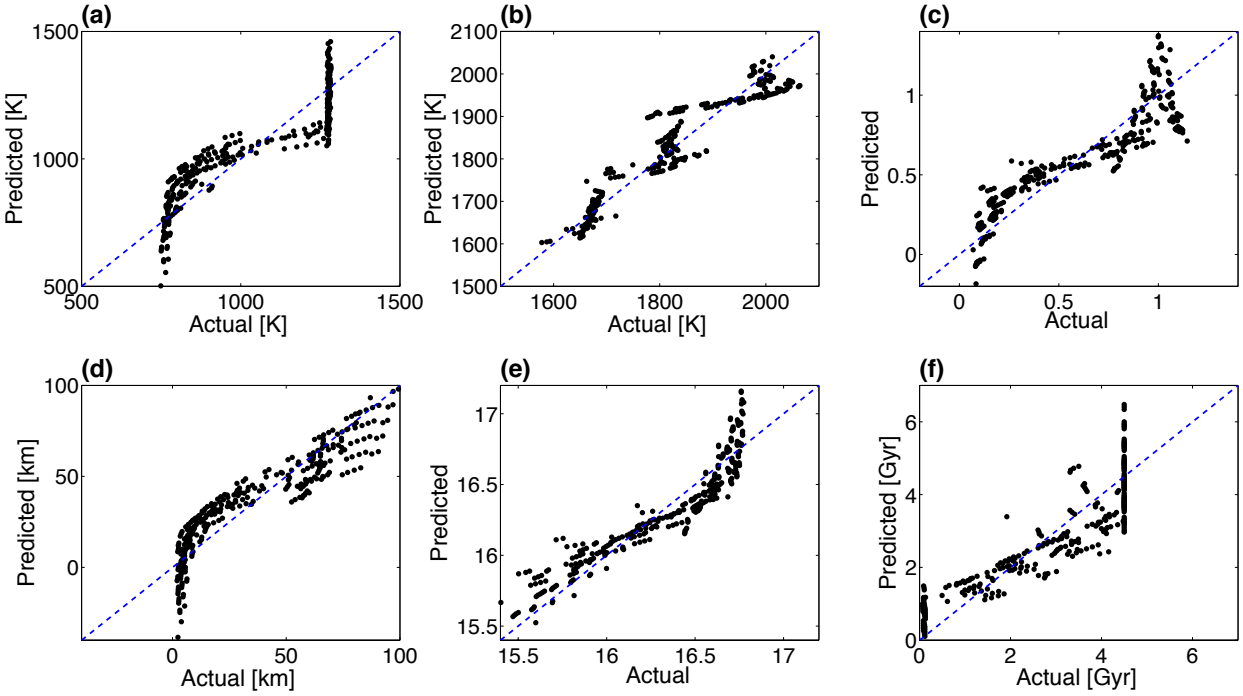

Figure 16: Plots showing correspondence between actual simulation output and values predicted using the best-fit linear function for 314 simulations of the thermal evolution of Venus. Panels represent (a) Moho temperature, (b) mantle potential temperature, (c) fraction of mantle processed by melting, (d) crustal thickness, (e) present-day atmospheric mass of radiogenic argon, and (f) the time at which core cooling, and thus plume upwelling, began to occur. The dashed blue line corresponds to perfect prediction.

conditions that satisfy three restrictions: $16.0294 \leq \log_{10}[M_{atm,Ar}(t_p)] \leq 16.3324$ (Kaula, 1999), $t_{plume} < 3.75$ Gyr, and 9 km $\leq h_c(t_p) \leq 75$ km. In these plots, simulations with initial conditions in the grey region are only expected to satisfy the constraint on the atmospheric mass of radiogenic argon. The dark grey region is for model outputs that both satisfy the argon constraint and the restriction on t_{plume}. Finally, the black region represents satisfaction of all three constraints. For a particular $T_{cm}(0)$, there is a limited range of $[\mathrm{U}(t_p)]_{PM}$ and $T_u(0)$ that are predicted to obey these constraints. Increasing $T_u(0)$, for instance, necessitates decreasing $[\mathrm{U}(t_p)]_{PM}$, and vice versa. With increasing $T_{cm}(0)$, the acceptable $[\mathrm{U}(t_p)]_{PM}$ and $T_u(0)$ both decrease.

Because the best-fit functions are only approximate, however, thermal evolution simulations must still be performed to double-check these predictions. For instance, a set of initial conditions indicated as acceptable by these contour plots is $[\mathrm{U}(t_p)]_{PM} = 15$ ppb, $T_u(0) = 1500$ K, and $T_{cm}(0) = 4000$ K. We set $f = 0.75$ to allow for mantle plume up-

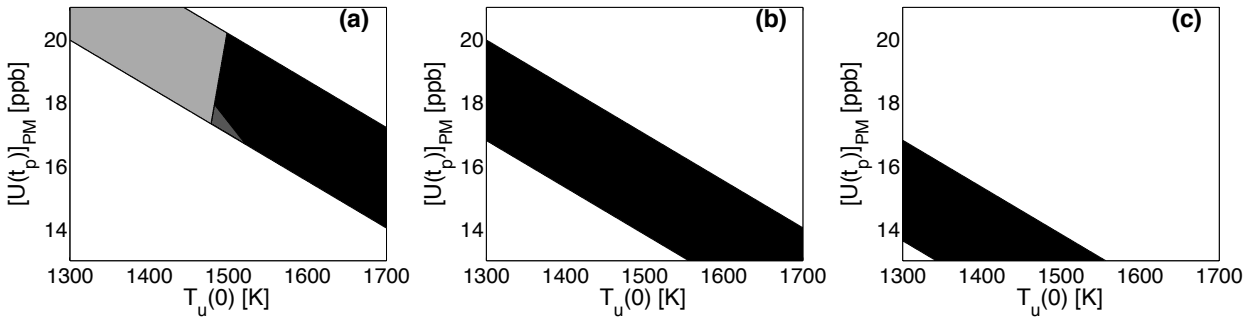

Figure 17: Contour plots showing initial conditions for the evolution of Venus that will produce the desired output. From left to right, $T_{cm}(0) = 3500$, 4000, and 4500 K. Default initial conditions are $\eta_0 = 10^{19}$ Pa s, $\Delta\eta_w = 100$, and $(d\rho/d\phi) = 120$ kg m^{-3}. Simulations in the light gray regions are predicted to be consistent with the present-day atmospheric mass of radiogenic argon, i.e., $16.0294 \leq \log_{10}[M_{atm,Ar}(t_p)] \leq 16.3324$. The dark gray regions indicate simulations that also have core cooling before 3.75 Gyr. The black regions represent simulations that further satisfy the final constraint 9 km $\leq h_c(t_p) \leq$ 75 km.

welling. Figure 18 shows the results of this simulation, compared to simulations with $[\mathrm{U}(t_p)]_{PM} = 21$ and 13 ppb. In the acceptable simulation, high temperatures from the transient "hot-start" in the core are lost within ∼100 Myr. Because the temperature of the mantle actually increases for ∼1.5 Gyr, core cooling is precluded until ∼3.75 Gyr. Present-day mantle potential temperature is not very sensitive to the choice of $[\mathrm{U}(t_p)]_{PM}$. Initial conditions, however, greatly affect crustal production.

In the simulation with $[\mathrm{U}(t_p)]_{PM} = 15$ ppb, crustal production occurs slowly for the first 2 Gyr of planetary evolution, eventually producing $h_c(t_p) \sim 15$ km. Moho temperatures always remain ∼200 K below the critical temperature for basal melting of the crust. The calculated atmospheric mass of radiogenic argon matches observations, and the estimated $[\mathrm{K}(t_p)]_{crust} \sim 0.6$ is consistent with the measurements from spacecraft landers. With the higher present-day uranium abundance of 21 ppb, crustal production occurs rapidly for ∼1 Gyr, and crustal temperatures increase quickly to the critical temperature for basal melting. Too much radiogenic argon is outgassed, although the final crustal abundance of potassium is actually lower than for the simulation with less radiogenic heating. With a low present-day uranium abundance of 13 ppb, too little radiogenic argon is outgassed. Furthermore, core cooling occurs at ∼3.0 Gyr. All three simulations predict similar present-day values of h_l and h_{TBL}.

Figure 19 shows the effect of mantle plumes on the argon budget and on melt production. Simulations were conducted with $[\mathrm{U}(t_p)]_{PM} = 15$ ppb, $T_u(0) = 1500$ K, and

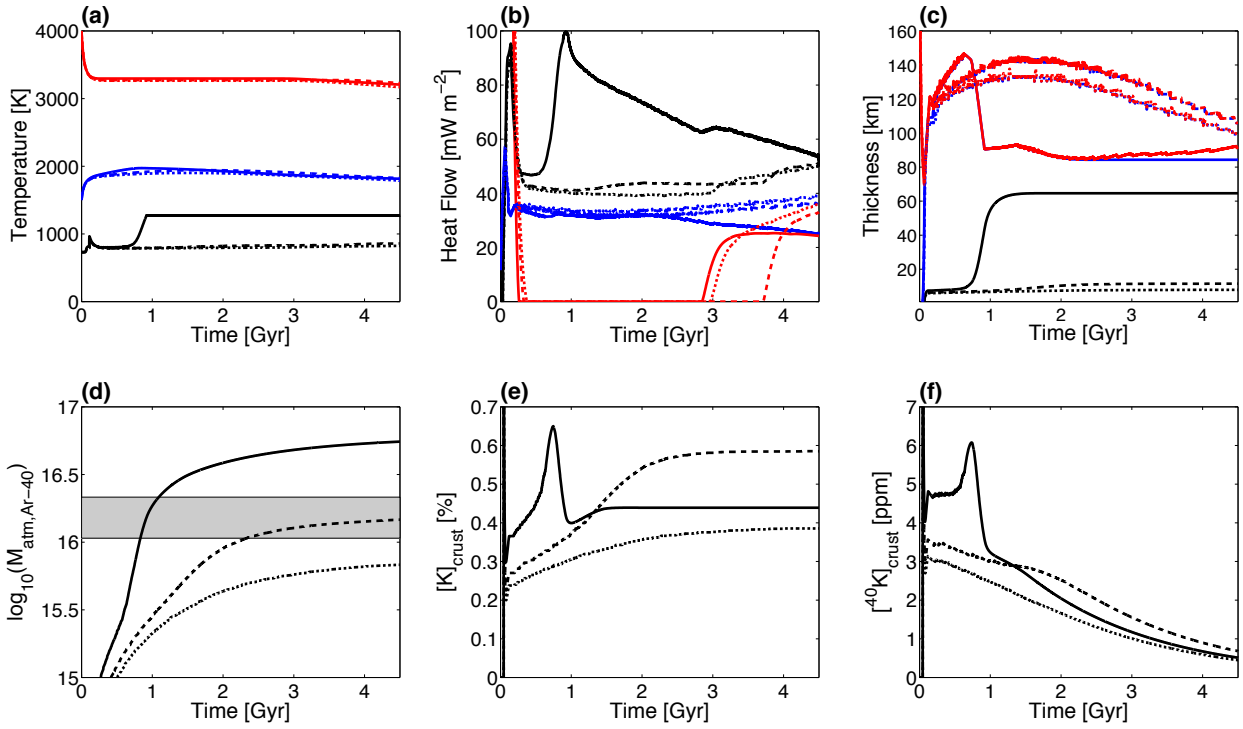

Figure 18: Thermal histories for Venus with $T_u(0) = 1500$ K and $T_{cm}(0) = 4000$ K. Red, blue, and black curves respectively signify (a) core/mantle boundary, mantle potential, and Moho temperatures; (b) surface, mantle, and core heat fluxes; (c) and crustal, depleted mantle lithosphere, and depleted mantle lithosphere thicknesses. Black lines also represent (d) mass of radiogenic argon in the atmosphere of Venus; (e) crustal concentration of potassium; and (f) crustal concentration of ^{40}K. The gray region in panel (d) indicates the present-day atmospheric mass of radiogenic argon. Solid, dashed, and dotted lines indicate $[\mathrm{U}(t_p)] = 21$, 15, and 13 ppb, respectively. The moving average of surface heat flux with a 75 Myr span is plotted because basal melting of the crust causes large discontinuities.

$T_{cm}(0) = 4000$ K for $f = 0.25$, 0.75, and 1. Although upwelling mantle plumes do contribute to the atmospheric mass of radiogenic argon, the mass of argon degassed from plumes is roughly nine orders of magnitude less than the mass degassed from ordinary sublithospheric convection. Because high mantle temperatures preclude core cooling except in the last ∼500 Myr, mantle plumes only occur during a relatively brief segment of the evolution of Venus. We assume that the heat flux out of the mantle from upwelling plumes must be less than or equal to the heat flux across the core/mantle boundary, although the thermal boundary layer at the core/mantle boundary contains enough hot material to produce a heat flux that is many orders of magnitude higher. This assumption causes the melt production from upwelling plumes to be much less than from sublithospheric con-

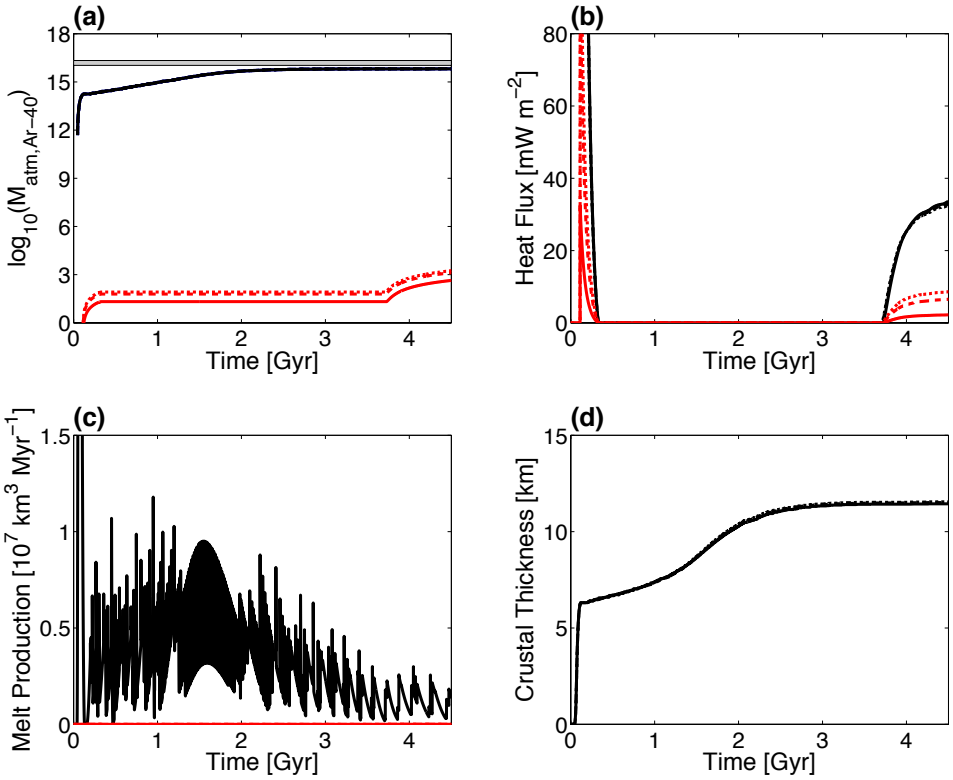

Figure 19: Simulation results with $[\mathrm{U}(t_p)]_{PM} = 15$ ppb, $T_u(0) = 1500$ K, $T_{cm}(0) = 4000$ K. Solid, dashed, and dotted lines represent and $f = 0.25$, 0.75, and 1, respectively. Panel (a) shows the mass of radiogenic argon in the atmosphere of Venus released from sublithospheric mantle melting (black) and upwelling plumes (red). The gray region is the measured present-day mass of atmospheric ^{40}Ar. Panel (b) shows the core heat flux (black) compared to the effective plume heat flux at the top of the mantle (red). Panel (c) plots the melt production from sublithospheric convection (black) and from upwelling plumes (red). Time series of crustal thickness are plotted in panel (d).

vection, which peaks at ∼1.75 Gyr but continues until the present. Figure 19 also shows that crustal production occurs most rapidly in the first ∼100 Myr of the simulation. Crust is produced at a moderate rate until the mantle potential temperature begins decreasing at ∼2 Gyr. As the mantle cools, crustal production proceeds relatively slowly until the present. Present-day crustal thicknesses consistent with the current atmospheric mass of radiogenic argon are generally between 10 and 15 km.

5 Discussion

Two end-member scenarios for the evolution of Venus yield different predictions of present-day crustal and lithosphere thicknesses. A single catastrophic resurfacing event that degasses a realistic amount of ^{40}Ar would produce crust between ∼15 and 50 km thick, with a corresponding lithosphere thickness between ∼300 and 1500 km. In contrast, models for continuous thermal evolution in the stagnant-lid regime predict much thinner crusts, i.e. $h_c < 15$ km. Mantle processing during stagnant-lid convection tends to sequester incompatible ^{40}K in the crust early in the evolution of Venus. Since all crustal argon is assumed to diffuse out into the atmosphere, a relatively high magnitude of argon is degassed. Unfortunately, the present-day crustal thickness of Venus is poorly constrained. Using gravity and topography data to construct a map of crustal thickness requires an estimate or guess of the mean crustal thickness. With an mean crustal thickness of ∼30 km, crustal thickness on Venus currently ranges from 21 to 75 km (Simons et al., 1997). But this solution is non-unique, and a much wider range of crustal thicknesses is plausible, although there is an upper limit of ∼200 km because thickness variations from topography in a thick crust would cause lateral flow, producing relaxation, which is not observed (Nimmo and Stevenson, 2001). Constraints on the thickness of the lithosphere of Venus are likewise loose; estimates range from as low as 80 km (Nimmo and McKenzie, 1998) to as high as 600 km (Orth and Solomatov, 2011).

The present-day atmospheric mass of radiogenic argon and the crustal abundance of potassium may allow the plausibility of different scenarios to be evaluated. In particular, a rapid resurfacing event satisfies the atmospheric argon constraint for $[\mathrm{U}(t_p]_{PM} = 21$ or 13 ppb, but no set of initial conditions for thermal evolution in the stagnant-lid regime will satisfy this constraint for $[\mathrm{U}(t_p]_{PM} = 21$ ppb and present-day K/U = 7220. Most previous studies assume $[\mathrm{U}(t_p]_{PM} = 21$ ppb (e.g., Kaula, 1999), but 13 ppb is a realistic lower bound for the Earth (Lyubetskaya and Korenaga, 2007), which allows thermal evolution simulations for Venus to produce a realistic amount of argon degassing. Especially since mantle convection, and thus argon degassing, must have occurred before a putative catastrophic resurfacing event, it is likely that the abundance of potassium in Venus is lower than previously assumed. Present-day crustal abundances of potassium that are predicted in both end-member scenarios are all consistent with data from spacecraft landers (Kaula, 1999). Precise measurements of the crustal abundance of ^{40}K have not yet been made.

Finding a satisfactory explanation for the young appearance of the surface of Venus is a critical problem. In Part I, we suggested that the formation of a self-destabilizing eclogite

layer may cause lithosphere floundering, but the phase transition from metamorphosed basalt to eclogite does not occur above 40 km depth on Venus. So, the formation of crust with sufficient thickness to invoke this mechanism would likely yield an unrealistically high magnitude of argon degassing. It is possible that argon is not incompatible as we have assumed (Watson et al., 2007), but this experimental result is not widely accepted (Cassata et al., 2011). Because simulations that match the atmospheric argon constraint tend to feature the resumption of core cooling at the same time that a resurfacing event is believed to have occurred, mantle plumes may play an important role. Upwelling mantle is already considered to be important to topographic rises, such as coronae, on the surface of Venus (Smrekar et al., 1997). The simulation results presented here feature relatively low melt production from mantle plumes, so this must be explored further in future work.

6 Conclusions

Matching models to observations is difficult. A number of constraints exist for the evolution of Venus, including measurements of the present-day atmospheric mass of radiogenic argon and estimates of the thicknesses of the crust and lithosphere. Furthermore, the vast majority of the surface of Venus is less than 750 Myr old. In this study, we investigate two end-member evolutionary scenarios that may explain these observations. A single catastrophic resurfacing event explains the young-looking surface of Venus and predicts realistic argon degassing for crustal thicknesses between 15 and 50 km. Argon degassing also is incorporated into a self-consistent model of stagnant-lid convection. Sensitivity analyses are used to explore the effects of initial conditions on model output, which are found to be reasonably approximated with a linear best-fit function. Using linear regression, a wide range of initial conditions that will produce a present-day Venus matching constraints on atmospheric argon and crustal thickness can be quantified. Compared to previous work, a lower initial abundance of heat-producing elements must be assumed. Interestingly, these simulations tend to feature a resumption of core cooling approximately when a resurfacing event is typically thought to have occurred. Upwelling mantle has long been recognized as important to the formation of coronae and other surface features on Venus, and we suggest that mantle plumes, along with magmatism from convection below the stagnant-lid, are a possible explanation for the young age of the Venusian surface.

Acknowledgments

I would like to thank Professor Korenaga for being a superlatively inspirational and supportive mentor. Without him, this work would not have been possible. Professor David Evans was very helpful in supplying guidelines for this thesis. The CT Space Grant Consortium and the George J. Schultz Fellowship from Yale University's Silliman College provided generous financial support.

References

Allègre, C.J., Hofmann, A., O'Nions, K., 1996. The argon constraints on mantle structure. Geophys. Res. Lett. 23, 3555–3557.

Bercovici, D., 2003. The generation of plate tectonics from mantle convection. Earth Planet. Sci. Lett. 205, 107–121.

Borucki, W.J., Koch, D.G., Basri, G., Batalha, N., Brown, T.M., Bryson, S.T., Caldwell, D., Christensen-Dalsgaard, J., Cochran, W.D., DeVore, E., Dunham, E.W., Gautier, III, T.N., Geary, J.C., Gilliland, R., Gould, A., Howell, S.B., Jenkins, J.M., Latham, D.W., Lissauer, J.J., Marcy, G.W., Rowe, J., Sasselov, D., Boss, A., Charbonneau, D., Ciardi, D., Doyle, L., Dupree, A.K., Ford, E.B., Fortney, J., Holman, M.J., Seager, S., Steffen, J.H., Tarter, J., Welsh, W.F., Allen, C., Buchhave, L.A., Christiansen, J.L., Clarke, B.D., Das, S., Désert, J.M., Endl, M., Fabrycky, D., Fressin, F., Haas, M., Horch, E., Howard, A., Isaacson, H., Kjeldsen, H., Kolodziejczak, J., Kulesa, C., Li, J., Lucas, P.W., Machalek, P., McCarthy, D., MacQueen, P., Meibom, S., Miquel, T., Prsa, A., Quinn, S.N., Quintana, E.V., Ragozzine, D., Sherry, W., Shporer, A., Tenenbaum, P., Torres, G., Twicken, J.D., Van Cleve, J., Walkowicz, L., Witteborn, F.C., Still, M., 2011. Characteristics of planetary candidates observed by Kepler. II. Analysis of the first four months of data. Astrophys. J. 736, doi:10.1088/0004–637X/736/1/19.

Bucher, K., Frey, M., 2002. Petrogenesis of Metamorphic Rocks. Springer-Verlag, Berlin. 7th edition.

Bullock, M.A., Grinspoon, D.H., 2001. The recent evolution of climate on Venus. Icarus 150, 19–37.

Byerlee, J., 1978. Friction of rocks. PAGEOPH 116, 615–625.

Cassata, W.S., Renne, P.R., Shuster, D.L., 2011. Argon diffusion in pyroxenes: Implications for thermochronometry and mantle degassing. Earth Planet. Sci. Lett. 304, 407–416, doi:10.1016/j.epsl.2011.02.019.

Charbonneau, D., Berta, Z.K., Irwin, J., Burke, C.J., Nutzman, P., Buchhave, L.A., Lovis, C., Bonfils, X., Latham, D.W., Udry, S., Murray-Clay, R.A., Holman, M.J., Falco, E.E.,

Winn, J.N., Queloz, D., Pepe, F., Mayor, M., Delfosse, X., Forveille, T., 2009. A super-Earth transiting a nearby low-mass star. Nature 462, 891–894, doi:10.1038/nature08679.

Christensen, U.R., 1985. Thermal evolution models for the Earth. J. Geophys. Res. 90, 2995–3007.

Davies, G.F., 1980. Thermal histories of convective Earth models and constraints on radiogenic heat production in the Earth. J. Geophys. Res. 85, 2517–2530.

Dziewonski, A.M., Anderson, D.L., 1981. Preliminary reference Earth model. Phys. Earth Planet. In. 25, 297–356.

Fowler, A.C., O'Brien, S.B.G., 1996. A mechanism for episodic subduction on Venus. J. Geophys. Res. 101, 4755–4763.

Fraeman, A.A., Korenaga, J., 2010. The influence of mantle melting on the evolution of Mars. Icarus 210, 43–57, doi:10.1016/j.icarus.2010.06.030.

Gershenfeld, N., 1998. The Nature of Mathematical Modeling. Cambridge University Press, New York.

Hauck, S.A., Phillips, R.J., 2002. Thermal and crustal evolution of Mars. J. Geophys. Res. 107, 5052, doi:10.1029/2001JE001801.

Hauck, S.A., Phillips, R.J., Price, M.H., 1998. Venus: Crater distribution and plains resurfacing models. J. Geophys. Res. 103, 13635–13642.

van Heck, H.J., Tackley, P.J., 2011. Plate tectonics on super-Earths: Equally or more likely than on Earth. Earth Planet. Sci. Lett. 310, 252–261, doi:10.1016/j.epsl.2011.07.029.

Herzberg, C., Condie, K., Korenaga, J., 2010. Thermal history of the Earth and its petrological expression. Earth Planet. Sci. Lett. 292, 79–88, doi:10.1016/j.epsl.2010.01.022.

Hirth, G., Kohlstedt, D.L., 1996. Water in the oceanic upper mantle: Implications for rheology, melt extraction and the evolution of the lithosphere. Earth Planet. Sci. Lett. 144, 93–108.

Jaupart, C., Labrosse, S., Mareschal, J.C., 2007. Temperatures, heat, and energy in the mantle of the Earth, in: Schubert, G. (Ed.), Treatise on Geophysics. Elsevier, New York. volume 1.

Karato, S.I., 2011. Rheological structure of the mantle of a super-Earth: Some insights from mineral physics. Icarus 212, 14–23, doi:10.1016/j.icarus.2010.12.005.

Kasting, J.F., Catling, D., 2003. Evolution of a habitable planet. Annu. Rev. Astro. Astrophys. 41, 429–463, doi:10.1146/annurev.astro.41.071601.170049.

Kaula, W.M., 1995. Venus reconsidered. Science 270, 1460–1464.

Kaula, W.M., 1999. Constraints on Venus evolution from radiogenic argon. Icarus 139, 32–29.

Kaula, W.M., Phillips, R.J., 1981. Quantitative tests for plate tectonics on Venus. Geophys. Res. Lett. 8, 1187–1190.

Kite, E.S., Manga, M., Gaidos, E., 2009. Geodynamics and rate of volcanism on massive Earth-like planets. Astrophys. J. 700, 1732–1749, doi:10.1088/0004–637X/700/2/173.

Korenaga, J., 2006. Archean geodynamics and the thermal evolution of Earth, in: Benn, K., Mareschal, J.C., Condie, K. (Eds.), Archean Geodynamics and Environments. American Geophysical Union, Washington, D.C., pp. 7–32.

Korenaga, J., 2007. Thermal cracking and the deep hydration of oceanic lithosphere: A key to the generation of plate tectonics? J. Geophys. Res. 112, B05408, doi:10.1029/2006JB004502.

Korenaga, J., 2008. Urey ratio and the structure and evolution of Earth's mantle. Rev. Geophys. 46, RG2007, doi:10.1029/2007RG000241.

Korenaga, J., 2009. Scaling of stagnant-lid convection with Arrhenius rheology and the effects of mantle melting. Geophys. J. Int. 179, 154–170, doi:10.1111/j.1365–246X.2009.04272.x.

Korenaga, J., 2010a. On the likelihood of plate tectonics on super-Earths: Does size matter? Astrophys. J. Lett. 725, L43–L46, doi:10.1088/2041–8205/725/1/L4.

Korenaga, J., 2010b. Scaling of plate-tectonic convection with pseudoplastic rheology. J. Geophys. Res. 115, B11405, doi:10.1029/2010JB007670.

Korenaga, J., Kelemen, P.B., Holbrook, W.S., 2002. Methods for resolving the origin of large igneous provinces from crustal seismology. J. Geophys. Res. 107, 2178, doi:10.1029/2001JB001030.

Landuyt, W., Bercovici, D., 2009. Variations in planetary convection via the effect of climate on damage. Earth Planet. Sci. Lett. 277, 29–37, doi:10.1016/j.epsl.2008.09.034.

Landuyt, W., Bercovici, D., Ricard, Y., 2008. Plate generation and two-phase damage theory in a model of mantle convection. Geophys. J. Int. 174, 1065–1080, doi:10.1111/j.1365–246X.2008.03844.x.

Léger, A., Rouan, D., Schneider, J., Barge, P., Fridlund, M., Samuel, B., Ollivier, M., Guenther, E., Deleuil, M., Deeg, H.J., Auvergne, M., Alonso, R., Aigrain, S., Alapini, A., Almenara, J.M., Baglin, A., Barbieri, M., Bruntt, H., Bordé, P., Bouchy, F., Cabrera, J., Catala, C., Carone, L., Carpano, S., Csizmadia, S., Dvorak, R., Erikson, A., Ferraz-Mello, S., Foing, B., Fressin, F., Gandolfi, D., Gillon, M., Gondoin, P., Grasset, O.,

Guillot, T., Hatzes, A., Hébrard, G., Jorda, L., Lammer, H., Llebaria, A., Loeillet, B., Mayor, M., Mazeh, T., Moutou, C., Pätzold, M., Pont, F., Queloz, D., Rauer, H., Renner, S., Samadi, R., Shporer, A., Sotin, C., Tingley, B., Wuchterl, G., Adda, M., Agogu, P., Appourchaux, T., Ballans, H., Baron, P., Beaufort, T., Bellenger, R., Berlin, R., Bernardi, P., Blouin, D., Baudin, F., Bodin, P., Boisnard, L., Boit, L., Bonneau, F., Borzeix, S., Briet, R., Buey, J.T., Butler, B., Cailleau, D., Cautain, R., Chabaud, P.Y., Chaintreuil, S., Chiavassa, F., Costes, V., Cuna Parrho, V., de Oliveira Fialho, F., Decaudin, M., Defise, J.M., Djalal, S., Epstein, G., Exil, G.E., Fauré, C., Fenouillet, T., Gaboriaud, A., Gallic, A., Gamet, P., Gavalda, P., Grolleau, E., Gruneisen, R., Gueguen, L., Guis, V., Guivarc'h, V., Guterman, P., Hallouard, D., Hasiba, J., Heuripeau, F., Huntzinger, G., Hustaix, H., Imad, C., Imbert, C., Johlander, B., Jouret, M., Journoud, P., Karioty, F., Kerjean, L., Lafaille, V., Lafond, L., Lam-Trong, T., Landiech, P., Lapeyrere, V., Larqué, T., Laudet, P., Lautier, N., Lecann, H., Lefevre, L., Leruyet, B., Levacher, P., Magnan, A., Mazy, E., Mertens, F., Mesnager, J.M., Meunier, J.C., Michel, J.P., Monjoin, W., Naudet, D., Nguyen-Kim, K., Orcesi, J.L., Ottacher, H., Perez, R., Peter, G., Plasson, P., Plesseria, J.Y., Pontet, B., Pradines, A., Quentin, C., Reynaud, J.L., Rolland, G., Rollenhagen, F., Romagnan, R., Russ, N., Schmidt, R., Schwartz, N., Sebbag, I., Sedes, G., Smit, H., , 2009. Transiting exoplanets from the CoRoT space mission VIII. CoRoT-7b: the first super-Earth with measured radius. Astro. Astrophys. 506, 287–302, doi:10.1051/0004–6361/200911933.

Lenardic, A., Jellinek, A.M., Moresi, L.N., 2008. A climate induced transition in the tectonic style of a terrestrial planet. Earth Planet. Sci. Lett. 271, 34–42, doi:10.1016/j.epsl.2008.03.031.

Lyubetskaya, T., Korenaga, J., 2007. Chemical composition of Earth's primitive mantle and its variance. J. Geophys. Res. 112, B03211, doi:10.1029/2005JB004223.

Mackwell, S.J., Zimmerman, M.E., Kohlstedt, D.L., 1998. High-temperature deformation of dry diabase with application to tectonics on Venus. J. Geophys. Res. 103, 975–984.

Mayor, M., Bonfils, X., Forveille, T., Delfosse, X., Udry, S., Bertaux, J.L., Beust, H., Bouchy, F., Lovis, C., Pepe, F., Perrier, C., Queloz, D., Santos, N.C., 2009. The HARPS search for southern extra-solar planets. Astro. Astrophys. 507, 487–494, doi:10.1051/0004–6361/200912172.

McKinnon, W.B., Zhanle, K.J., Ivanov, B.A., Melosh, J.H., 1997. Cratering on Venus: Models and observations, in: Venus II. Arizona Univ. Press, pp. 969–1014.

Moresi, L.N., Solomatov, S., 1998. Mantle convection with a brittle lithosphere: thoughts on the global tectonic styles of the Earth and Venus. Geophys. J. Int. 133, 669–682.

Namiki, N., Solomon, S.C., 1998. Volcanic degassing of argon and helium and the history of crustal production on Venus. J. Geophys. Res. 103, 3655–3677.

Nimmo, F., McKenzie, D., 1998. Volcanism and tectonics on Venus. Annu. Rev. Earth Planet. Sci. 26, 23–51, doi:10.1146/annurev.earth.26.1.23.

Nimmo, F., Stevenson, D.J., 2001. Estimates of Martian crustal thickness from viscous relaxation of topography. J. Geophys. Res. 106, 5085–5098.

Noack, L., Breuer, D., Spohn, T., 2012. Coupling the atmosphere with interior dynamics: Implications for the resurfacing of Venus. Icarus 217, 484–498, doi:10.1016/j.icarus.2011.08.026.

O'Neill, C., Lenardic, A., 2007. Geological consequences of super-sized Earths. Geophys. Res. Lett. 34, L19204, doi:10.1029/2007GL030598.

Orth, C.P., Solomatov, V.S., 2011. The isostatic stagnant lid approximation and global variations in the Venusian lithosphere thickness. Geochem. Geophys. Geosyst. 12, Q07018, doi:10.1029/2011GC003582.

Phillips, R.J., Bullock, M.A., Hauck, S.A., 2001. Climate and interior coupled evolution on Venus. Geophys. Res. Lett. 28, 1779–1782.

Phillips, R.J., Hansen, V.L., 1998. Geological evolution of Venus: Rises, plains, plumes, and plateaus. Science 279, 1492–1497, doi:10.1126/science.279.5356.1492.

Philpotts, A., Ague, J.J., 2009. Principles of Igneous and Metamorphic Petrology. Cambridge University Press. 2nd edition.

Queloz, D., Bouchy, F., Moutou, C., Hatzes, A., Hébrard, G., Alonso, R., Auvergne, M., Baglin, A., Barbieri, M., Barge, P., Benz, W., Bordé, P., Deeg, H.J., Deleuil, M., Dvorak, R., Erikson, A., Ferraz Mello, S., Fridlund, M., Gandolfi, D., Gillon, M., Guenther, E., Guillot, T., Jorda, L., Hartmann, M., Lammer, H., Léger, A., Llebaria, A., Lovis, C., Magain, P., Mayor, M., Mazeh, T., Ollivier, M., Pätzold, M., Pepe, F., Rauer, H., Rouan, D., Schneider, J., Segransan, D., Udry, S., Wuchterl, G., 2009. The CoRoT-7 planetary system: two orbiting super-Earths. Astro. Astrophys. 506, 303–319, doi:10.1051/0004–6361/200913096.

Reese, C.C., Solomatov, V.S., Moresi, L.N., 1999. Non-Newtonian stagnant lid convection and magmatic resurfacing on Venus. Icarus 139, 67–80.

Ringwood, A.E., 1991. Phase transformations and their bearing on the constitution and dynamics of the mantle. Geochim. Cosmochim. Acta 55, 2083–2110.

Rivera, E.J., Lissauer, J.J., Butler, R.P., Marcy, G.W., Vogt, S.S., Fischer, D.A., Brown, T.M., Laughlin, G., Henry, G.W., 2005. A $7.5M_{\oplus}$ planet orbiting the nearby star, GJ 876. Astrophys. J. 634, 625–640, doi:10.1086/491669.

Romeo, I., Turcotte, D.L., 2010. Resurfacing on Venus. Planet. Space Sci. 58, 1374–1380, doi:10.1016/j.pss.2010.05.022.

Schaber, G.G., Strom, R.G., Moore, H.J., Soderblom, L.A., Kirk, R.L., Chadwick, D.J., Dawson, D.D., Gaddis, L.R., Boyce, J.M., Russell, J., 1992. Geology and distribution of impact craters on Venus: What are they telling us? J. Geophys. Res. 97, 13257–13301.

Schubert, G., Solomon, S.C., Turcotte, D.L., Drake, M.J., Sleep, N.H., 1992. Origin and thermal evolution of Mars, in: Kieffer, H.H., Jakosky, B.M., Snyder, C.W., Matthews, M.S. (Eds.), Mars. University of Arizona Press, Tucson, AZ, pp. 147–183.

Schubert, G., Stevenson, D.J., Cassen, P., 1980. Whole planet cooling and the radiogenic heat source contents of the Earth and Moon. J. Geophys. Res. 85, 2531–2538.

Schubert, G., Turcotte, D.L., Olson, P., 2001. Mantle Convection in the Earth and Planets. Cambridge University Press, New York.

Seager, S., Kuchner, M., Hier-Majumder, C.A., Militzer, B., 2007. Mass-radius relationships for solid exoplanets. Astrophys. J. 669, 1279–1297, doi:10.1086/521346.

Shaw, D.M., 1970. Trace element fractionation during anatexis. Geochim. Cosmochim. Acta 34, 237–243.

Simons, M., Solomon, S.C., Hager, B.H., 1997. Localization of gravity and topography: constraints on the tectonics and mantle dynamics of Venus. Geophys. J. Int. 131, 24–44.

Smrekar, S.E., Kiefer, W.S., Stofan, E.R., 1997. Large volcanic rises on Venus, in: Bougher, S.W., Hunten, D.M., Phillips, R.J. (Eds.), Venus II: Geology, geophysics, atmosphere, and solar wind environment. University of Arizona Press, pp. 845–878.

Smrekar, S.E., Stofan, E.R., Mueller, N., Treiman, A., Elkins-Tanton, L., Helbert, J., Piccioni, G., Drossart, P., 2010. Recent hotspot volcanism on Venus from VIRTIS emissivity data. Science 328, 605–608, doi:10.1126/science.1186785.

Solomatov, V.S., 1995. Scaling of temperature- and stress-dependent viscosity convection. Phys. Fluids 7, 266–274.

Solomatov, V.S., Moresi, L.N., 1996. Stagnant lid convection on venus. J. Geophys. Res. 101, 4737–4753.

Solomatov, V.S., Moresi, L.N., 2000. Scaling of time-dependent stagnant lid convection: Application to small-scale convection on Earth and other terrestrial planets. J. Geophys. Res. 105, 21795–21817, doi:10.1029/2000JB900197.

Sotin, C., Grasset, O., Mocquet, A., 2007. Mass-radius curve for extrasolar Earth-like planets and ocean planets. Icarus 191, 337–351, doi:10.1016/j.icarus.2007.04.006.

Spohn, T., 1991. Mantle differentiation and thermal evolution of Mars, Mercury, and Venus. Icarus 90, 222–236.

Stamenkovic, V., Breuer, D., Spohn, T., 2011. Thermal and transport properties of mantle rock at high pressure: Applications to super-Earths. Icarus 216, 572–596, doi:10.1016/j.icarus.2011.09.030.

Stamenkovic, V., Noack, L., Breuer, D., Spohn, T., 2012. The influence of pressure-dependent viscosity on the thermal evolution of super-Earths. Astrophys. J. 748, doi:10.1088/0004–637X/748/1/41.

Stevenson, D.J., 2003. Styles of mantle convection and their influence on planetary evolution. C. R. Geoscience 335, 99–111.

Stevenson, D.J., Spohn, T., Schubert, G., 1983. Magnetism and thermal evolution of the terrestrial planets. Icarus 54, 466–489.

Strom, R.G., Schaber, G.G., Dawson, D.D., 1994. The global resurfacing of Venus. J. Geophys. Res. 99, 10899–10926.

Turcotte, D.L., 1993. An episodic hypothesis for Venusian tectonics. J. Geophys. Res. 98, 17061–17068.

Turcotte, D.L., Schubert, G., 2002. Geodynamics. Cambridge University Press, Cambridge. 2nd edition.

Udry, S., Bonfils, X., Delfosse, X., Forveille, T., Mayor, M., Perrier, C., Bouchy, F., Lovis, C., Pepe, F., Queloz, D., Bertaux, J.L., 2007. The HARPS search for southern extra-solar planets XI. Super-Earths in a 3-planet system. Astro. Astrophys. 469, L43–L47, doi:10.1051/0004–6361:20077612.

Valencia, D., O'Connell, R.J., Sasselov, D., 2006. Internal structure of massive terrestrial planets. Icarus 181, 545–554.

Valencia, D., O'Connell, R.J., Sasselov, D., 2007. Inevitability of plate tectonics on super-Earths. Astrophys. J. 670, L45–L48, doi:10.1086/524012.

Vlaar, N.J., van Keken, P.E., van den Berg, A.P., 1994. Cooling of the Earth in the Archaean: Consequences of pressure-release melting in a hotter mantle. Earth Planet. Sci. Lett. 121, 1–18.

Wagner, F.W., Sohl, F., Hussmann, H., Grott, M., Rauer, H., 2011. Interior structure models of solid exoplanets using material laws in the infinite pressure limit. Icarus 214, 366–376, doi:10.1016/j.icarus.2011.05.027.

Watson, E.B., Thomas, J.B., Cherniak, D.J., 2007. ^{40}Ar retention in the terrestrial planets. Nature 449, 299–304, doi:10.1038/nature06144.

Weizman, A., Stevenson, D.J., Prialnik, D., Podolak, M., 2001. Modeling the volcanism on Mars. Icarus 150, 195–205.